RESEARCH ARTICLE

Warm conveyor belts as amplifiers of forecast uncertainty

Moritz Pickl (Deinhard) | **Julian F. Quinting** | **Christian M. Grams**

Institute of Meteorology and Climate
Research (IMK–TRO), Department
Troposphere Research, Karlsruhe Institute
of Technology (KIT), Karlsruhe, Germany

Correspondence
Moritz Pickl (Deinhard), Karlsruher
Institut für Technologie (KIT), Institut für
Meteorologie und Klimaforschung,
Postfach 3640, 76021 Karlsruhe, Germany.
Email: moritz.deinhard@gmail.com

Funding information
Helmholtz Association, Grant/Award
Number: VH-NG-1243

Abstract

Warm conveyor belts (WCBs) are rapidly ascending air streams associated with extratropical cyclones. WCBs exert a substantial influence on the evolution of the large-scale midlatitude flow and have previously been related to increased forecast uncertainty in case studies. This study provides a first systematic investigation of the role of WCBs for errors in medium-range ensemble forecasts in the Atlantic–European region. The study is enabled through a unique data set, allowing for a Lagrangian detection of WCBs in three years of operational ensemble forecasts from the European Centre for Medium-Range Weather Forecasts. By analysing the relationship between commonly used error metrics of variables that characterise the large-scale flow and WCBs, the study aims to shed light on the question of the extent to which WCBs act as a source of forecast errors and as an amplifier of pre-existing errors in a state-of-the-art global operational numerical weather prediction model. We show that forecasts with high WCB activity are on average characterised by an amplified Rossby-wave pattern and anticyclonic flow anomalies downstream. We find that the forecast skill is generally reduced when the WCB activity is high, and that WCB activity is particularly increased when the error growth is largest. To establish a causal relationship, we employ two composite approaches. The first focuses on the time of largest error growth and the second calculates normalised forecast error fields centered on WCB objects. Both approaches yield a consistent picture: anomalously high errors are initially associated with misrepresentations of an upstream trough. In regions of WCB ascent and outflow, the errors grow rapidly in terms of magnitude and scale and are projected onto the upper-level large-scale circulation. We also find indications that WCBs can cause errors even when the upstream flow is well represented. Notwithstanding, evidence is robust for WCBs acting as an amplifier of forecast uncertainty.

KEYWORDS
composite analysis, forecast error, forecast uncertainty, trajectory analysis, warm conveyor belts

1 | INTRODUCTION

Warm conveyor belts (WCBs) are coherent, moist air streams that originate from the warm sector of extratropical cyclones and ascend from the boundary layer into the upper troposphere (Carlson, 1980). Initially driven by dry dynamic forcing, which is described well by quasigeostrophic (QG) theory (Binder *et al.*, 2016), the air ascends adiabatically along the cold front until saturation is reached. The condensation of water vapor then leads to the formation of an elongated cloud band that is associated with large amounts of precipitation (Pfahl *et al.*, 2014). The cloud-diabatic processes during the ascent result in the release of latent heat, which further enhances the ascending motion from the lower into the upper troposphere through cross-isentropic air-mass transport.

WCBs substantially affect the evolution of the extratropical circulation, as the diabatic heating is associated with the formation of lower and upper tropospheric potential vorticity (PV) anomalies: underneath and close to the latent heating maximum in the mid troposphere, a cyclonic PV anomaly is produced, which potentially affects the strength and life cycle of the surface cyclone (Dacre and Gray, 2013; Binder *et al.*, 2016; Martínez-Alvarado *et al.*, 2016a). In the upper troposphere, above the heating maximum, PV is destroyed (Wernli and Davies, 1997; Pomroy and Thorpe, 2000), so that the net change of PV from the inflow to the outflow of WCBs is close to zero (Madonna *et al.*, 2014b; Methven, 2015). The net effect of the cross-isentropic motion of WCBs is thus to transport low-PV air poleward and upward, leading to anticyclonic anomalies in the upper troposphere (Wernli and Davies, 1997; Grams *et al.*, 2013; Madonna *et al.*, 2014b). When this diabatically heated, divergent outflow of WCBs impinges on the upper-level wave guide and jet stream, the wave guide is deflected polewards, resulting in an amplification of the upper-level flow and ridge building (Grams *et al.*, 2011; Chagnon *et al.*, 2013; Martínez-Alvarado *et al.*, 2016b). The low-PV outflow additionally enhances the PV gradient across the tropopause and thereby results in the formation of a jet streak (Grams *et al.*, 2013; Grams and Archambault, 2016). The ridge amplification can subsequently lead to the downstream development and propagation of baroclinic Rossby-wave packets (Röthlisberger *et al.*, 2018) and contribute to Rossby-wave breaking events (Madonna *et al.*, 2014a). Recent studies further highlight the role of WCB outflow for the formation and maintenance of atmospheric blocking (e.g., Pfahl *et al.*, 2015; Steinfeld and Pfahl, 2019).

In turn, the characteristics of the WCB ascent and the subsequent modulation of the large-scale flow are sensitive to the environmental conditions, such as the low-level moisture supply in the inflow region (Schäfler and Harnisch, 2015; Berman and Torn, 2019), the low-level baroclinicity (Grams *et al.*, 2018), or the upper-level forcing (Binder *et al.*, 2016). Due to the combination of these WCB sensitivities to the atmospheric conditions and their impact on the evolution of the synoptic- to planetary-scale flow, WCBs serve as a dynamical link between different scales and the lower and upper levels of the troposphere. The existence of this dynamic link is underpinned by the fact that flow situations with WCB activity have been shown to be associated with increased forecast uncertainty due to two different mechanisms.

- Due to their pronounced sensitivity to the environmental conditions, WCBs can project small-scale (initial condition) errors onto the large-scale flow (Grams *et al.*, 2018), where they grow rapidly along the midlatitude wave guide. This mechanism is formally known as upscale error growth and has been described in a conceptual three-stage model (Zhang *et al.*, 2007): during the first hours of the forecast integration, localised, small-scale errors from the initial conditions grow to the convective scale. In a second stage, the errors in convective-scale unbalanced flow are projected onto the large scale via geostrophic adjustment (Bierdel *et al.*, 2018), resulting in errors in the balanced flow field, which finally amplify with dry dynamic barotropic Rossby-wave activity (Baumgart *et al.*, 2019) and baroclinic instability (Davies and Didone, 2013). Moist diabatic processes related to WCB activity have been shown to play an important role in the second stage of upscale error growth (Baumgart *et al.*, 2019).

- The cloud-diabatic processes that govern the ascent of WCBs occur on the subgrid scale of current global numerical weather prediction models and therefore have to be parametrised. The parametrisations of physical processes, however, are associated with forecast uncertainty (Leutbecher *et al.*, 2017). Several studies investigated the sensitivities of WCBs to the choice of different parametrisation schemes and found that the WCB ascent characteristics and the impact on the downstream flow evolution depend on the applied microphysics (e.g. Joos and Forbes, 2016; Mazoyer *et al.*, 2021; Choudhary and Voigt, 2022) and convection (Rivière *et al.*, 2021) schemes. Further, Pickl *et al.* (2022) found sensitivities of WCBs to stochastic perturbations of physical processes. This indicates that WCBs can act as a direct source of forecast uncertainty, additionally to the propagation and amplification of pre-existing forecast errors through upscale error growth.

Even though, conceptually, these two mechanisms can be described independently from each other, in practice

they overlap. For example, the quality of the data assimilation can be compromised during situations with WCB activity (i.e., reduction of assimilated satellite observations through cloud cover), which favors subsequent upscale error growth. Further, the two mechanisms can also happen at the same time and are therefore nontrivial to separate.

As WCBs are inherently coupled to extratropical cyclones that involve both dry baroclinic and moist diabatic processes, disentangling both is a challenging task. One might argue that dry dynamics is a main driver of error growth and WCB-related errors occur as a byproduct. However, there is extensive evidence in the literature that WCBs provide an important contribution to large-scale flow amplification and—based on case studies—error growth. Experiments suppressing latent heating and thereby upper-level diabatic outflow related to WCBs reveal a much weaker amplification of the downstream ridge and Rossby-wave pattern, partly missing the onset of blocking (e.g., Grams and Archambault, 2016, Steinfeld et al., 2020). In a PV-tendency framework, Teubler and Riemer (2021) show that the divergent flow component can be interpreted as an indirect moist diabatic process, which contributes substantially to ridge amplification. Furthermore, the divergent flow only contains a minor dry dynamic component during ridge amplification (Quinting and Jones, 2016; Steinfeld and Pfahl, 2019). We therefore use WCBs as proxy metric for moist baroclinic development. With regard to forecast errors, Grams et al. (2018), Baumgart and Riemer (2019), and Sánchez et al. (2020) provide case-study evidence that the local amplification of forecast uncertainty in situations of ridge building/amplification can be dominated by the divergent flow related to WCBs.

Typically, WCBs are detected by computing trajectories from gridded data sets and only those trajectories that reflect distinct ascent behavior are retained, for example, by applying a threshold criterion of an ascent or latent heating rate (Wernli, 1997; Madonna et al., 2014b). This Lagrangian detection of WCBs requires a minimum spatial resolution of the input fields, especially in the vertical, which is typically not provided in commonly available forecast archives (Bowman et al., 2013). Therefore, systematic evaluations of WCBs in forecast data sets and their role for forecast uncertainty are very rare, and most studies either choose a case study approach (e.g. Joos and Forbes, 2016; Grams et al., 2018; Berman and Torn, 2019; Oertel et al., 2023) and/or use Eulerian metrics to quantify the impact of WCBs on the upper-level flow indirectly (e.g. Baumgart and Riemer, 2019; Sánchez et al., 2020). Madonna et al. (2015) provide a first systematic verification of trajectory-based WCBs in deterministic high-resolution forecasts of the European Centre

for Medium-Range Weather Forecasts (ECMWF). Even though they were able to link individual periods of reduced forecast skill to misrepresentations of WCBs, they did not establish a systematic relationship between WCBs and forecast errors. The recent development of statistical (Quinting and Grams, 2021) and machine-learning based techniques (Quinting and Grams, 2022) to identify WCB footprints from various gridded datasets (Quinting et al., 2022) enabled the first systematic evaluation of the representation of WCBs in a reforecast data set, where it was shown that forecasts with high WCB activity have on average reduced forecast skill compared with forecasts with low WCB activity (Wandel et al., 2021).

Despite this extensive literature catalogue on the role of WCBs in the evolution of the large-scale extratropical circulation, so far no process-based, systematic evaluation of the relationship between WCBs and forecast errors has been provided. This study attempts to establish a causal relationship by adopting different perspectives on the co-occurrence of trajectory-based WCB footprints and medium-range forecast errors (up to 10 days lead) in a unique archive of operational ensemble forecasts. In doing so, the study sheds light on the question of whether a WCB and the chain of processes associated with it—from a process-oriented perspective—can be considered as a source or an amplifier of forecast errors in a state-of-the-art operational weather prediction model. This study is structured as follows. After a detailed description of the data set and methods in Section 2, the climatological co-occurrence of WCBs and forecast errors (Section 3.1) and forecast error growth (Section 3.2) is evaluated. In Section 3.3, a composite technique is applied to center forecast errors on objectively detected WCB objects, and the findings of the study are discussed in the context of existing literature and conclusions drawn in Section 4.

2 | DATA AND METHODS

2.1 | ECMWF ensemble forecasts

We use three years of operational medium-range ECMWF ensemble forecasts initialised twice daily (0000 and 1200 UTC) in winter (DJF) between December 1, 2018 and February 28, 2021. The forecasts are run on a TCo639 grid equivalent to a horizontal resolution of approximately 18 km in the extratropics and with 91 vertical levels, and are retrieved until a lead time of 12 days on a regular $1° \times 1°$ latitude–longitude grid and at a six-hourly temporal resolution in a domain ranging from the North American west coast to eastern Europe (15°–80° N, 130° W–80° E). With 50 perturbed and one unperturbed ensemble member, the data set consists of more than 27,000 individual

forecasts. The trajectory computation for WCB detection requires data on model levels that are not archived operationally at ECMWF. This has, so far, hindered a systematic evaluation of WCBs in forecast data sets. In the past years we have therefore collected a unique data set by retrieving model level data from operational ECMWF ensemble forecasts continuously in near-real time and archiving the data locally.

2.2 | WCB detection

We use the Lagrangian Analysis Tool (Lagranto; Wernli and Davies, 1997; Sprenger and Wernli, 2015) to detect footprints of WCBs in the ensemble forecasts and the analyses. Based on six-hourly input fields, we compute 48-hr forward trajectories from starting points seeded on a 100-km equidistant grid on seven equally spaced pressure levels between 1000 and 700 hPa. Subsequently, only those trajectories that ascend by at least 600 hPa within 48 hr are retained and identified as WCB trajectories. The four-dimensional (latitude, longitude, pressure, time) trajectory objects are gridded to a binary two-dimensional field by assigning each trajectory point at the corresponding valid time to an inflow (pressure > 800 hPa), ascent (800 hPa > pressure > 400 hPa), or outflow (pressure < 400 hPa) layer. A circle with a radius of 100 km is drawn around the trajectory positions in every height layer, and each grid point on a regular 1° × 1° grid that lies within this circle is assigned the value 1 (same technique as applied in Madonna *et al.* (2014b) and Pickl *et al.* (2022)).

2.3 | Forecast error evaluation and variable selection

The forecast error is expressed in terms of the root-mean squared error (RMSE), which is defined as

$$RMSE = \sqrt{\frac{1}{N}\sum_{i=1}^{N}(F_i - O_i)^2}, \qquad (1)$$

with F_i being the predicted value at grid point i, O_i the corresponding verifying analysis, and N the number of grid points in the verification domain. The RMSE is computed for each ensemble member and applied to two meteorological fields: geopotential height at 500 hPa ($Z500$), which is a well-established variable to evaluate forecast skill, and the wind speed at model level 52 (corresponding to a pressure of approximately 250 hPa, $WS250$), which is used to evaluate forecast errors at the level of WCB outflow. The latter ($WS250$) has been chosen in order to avoid the costly

interpolation of our archived model-level data to pressure levels or the download of additional fields. As verifying analysis, we use the unperturbed control forecast at lead time 0 hr for the valid times 0000 and 1200 UTC and at lead time 6 hr for the valid times 0600 and 1800 UTC. This ensures consistent vertical levels of the forecast and the verifying analysis for $WS250$, which would not be given for the operational high-resolution analysis or the ERA5 reanalysis (these both have 137 vertical levels).

2.4 | WCB-centered composites

In Section 3.3, forecast errors related to WCBs are evaluated by computing WCB-centered composites of RMSE. These are constructed in the following way.

At first, WCB objects are detected as contiguous regions of grid points that are associated with footprints of WCB ascent or outflow obtained from the trajectory-gridding procedure described above. The size distribution of the WCB ascent (green line in Figure 1) and outflow (blue line in Figure 1) objects shows that 50% of the outflow objects are smaller than 81,000 km² (i.e., 0.081×10⁶ km²; see colored vertical lines in Figure 1). Further, the ascent objects are on average smaller than the outflow objects, which is reflected mainly in the longer tail of the distribution of outflow objects. In order to consider only those WCB objects that are relevant for the modification of the large-scale flow, only objects with a minimum size of 300,000 km² are taken into account (which is equivalent to about 35 grid cells at a mean latitude of 45°N; for reference, the area of the UK is about 250,000 km²). This threshold is to some extent arbitrary and was chosen based on a visual inspection of individual cases. The value of 300,000 km² corresponds to the 78th percentile of the ascent objects and to the 75th percentile of the outflow objects, respectively. This detection is performed in all 27,000 individual forecasts for lead times between 72 and 168 hr, resulting in about 550,000 ascent and about 750,000 outflow objects distributed across the entire data set. The lead-time range is chosen such that data are available from three days prior until three days after WCB objects have been detected.

For the evaluation of WCB-centered composites, the center of mass is then determined for each object. Note that the grid point to which the center of mass is assigned does not necessarily lie within a WCB object (e.g., in the case of arch-shaped outflow objects that sometimes occur). Subsequently, the coordinates of a 40° × 60° latitude–longitude box around the center of mass are extracted. This procedure is illustrated in Figure 2 for outflow objects in one arbitrarily chosen situation. In the example shown, only objects with IDs 2 and 6 are retained; all other objects are smaller than the selection threshold. Note that no object
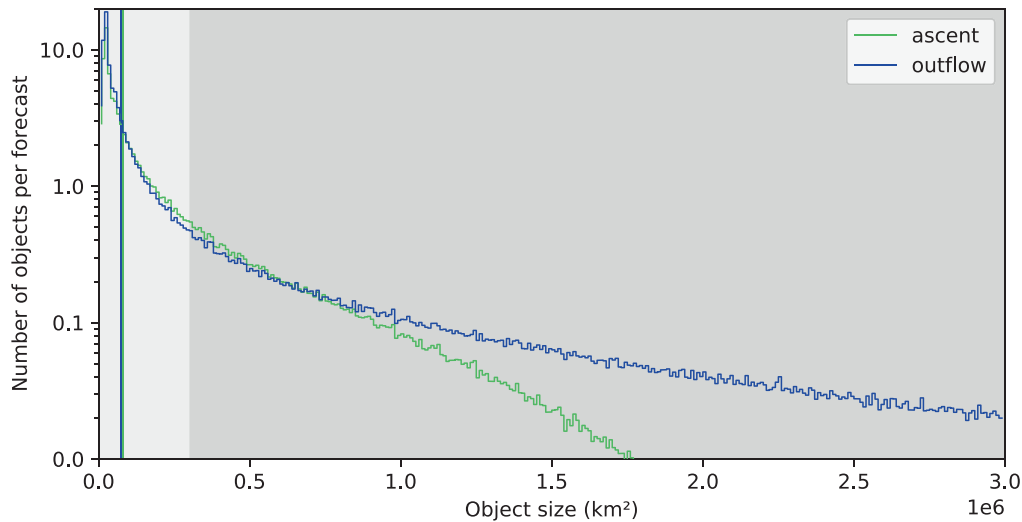
FIGURE 1 Size distribution of WCB ascent (green) and outflow (blue) objects with centers of mass lying within the North Atlantic domain (80°W–20°E, 30°–90°N), as detected in the ensemble data set. The dark gray shading denotes the size range in which WCB objects are considered. The bin width is 10,000 km². The colored vertical lines show the median size of the ascent (green) and outflow (blue) masks. The counts are normalised by the number of forecasts in the data set, resulting in the average number of objects of the corresponding size per 168-hr forecast. Note the logarithmic scale on the *y*-axis. [Colour figure can be viewed at wileyonlinelibrary.com]

tracking has been performed, which means that objects associated with the same feature can be identified multiple times at subsequent time steps. All forecast objects fulfilling the size prescription are considered, regardless of whether there is a corresponding object in the analysis. We have performed sensitivity tests with several different algorithms and found that a more scrutinised matching of forecast and analysis WCB objects does not affect the results based on the WCB-centered composites (see Supporting Information Figures S1 and S2). The coordinates of the 40° × 60° latitude–longitude box are then used to compute composites of different variables centered on the WCB objects with time lags of three days prior to three days after the detection. For computation of the composites, only those WCB objects with center of mass located within the domain 80°W–20°E, 30°–90°N are considered (i.e., the region where both WCB occurrence and forecast errors are largest, see Figure 3).

The composites are calculated for three different types of variables: WCB footprints of inflow, ascent, and outflow, meteorological variables (mean sea-level pressure (MSLP), $Z500$, $WS250$) and the RMSE of $Z500$ and $WS250$. The WCB footprints are absolute frequencies (0–1 masks) and can therefore be composited without any further steps. The meteorological fields, as well as the RMSE, however, vary spatially (and the RMSE also with forecast lead time), which requires a normalisation when composite members with different coordinates and lead times are compared. For the meteorological fields, this is done by subtracting the three-year DJF model climatology (seasonal (DJF) climatology for the considered years

2018/2019, 2019/2020, and 2020/2021 averaged across all lead times from 0–240 hr) from the full field at the corresponding grid points, which yields an anomaly. To normalise the RMSE, the instantaneous RMSE is divided by the corresponding three-year DJF model climatology (determined for the grid point and lead time) of the RMSE. This results in a range between 0 and ∞, where values larger than one correspond to anomalously large errors and values below one denote errors smaller than usual. This method follows the one from Aiyyer (2015), who performed a similar analysis with extratropical transitions of tropical cyclones (ETs). Note that this centered-composite approach is not used until Section 3.3; in the analysis steps before, all variables (WCB frequencies, $Z500$ and $WS250$ fields, and error fields) are used without spatial centering.

3 | RESULTS

3.1 | Spatial co-occurrence of climatological WCBs and forecast error

To address the question of whether WCBs affect the forecast performance systematically, we first analyse the average spatial patterns of forecast errors and WCB occurrence (see Figure 3). The three-year DJF model climatology of $Z500$ (see Figure 3a) is characterised by a trough over the western North Atlantic and a ridge over the eastern North Atlantic and Europe. In particular, the central to eastern North Atlantic is associated with large variability (black contours). An elongated band of large climatological
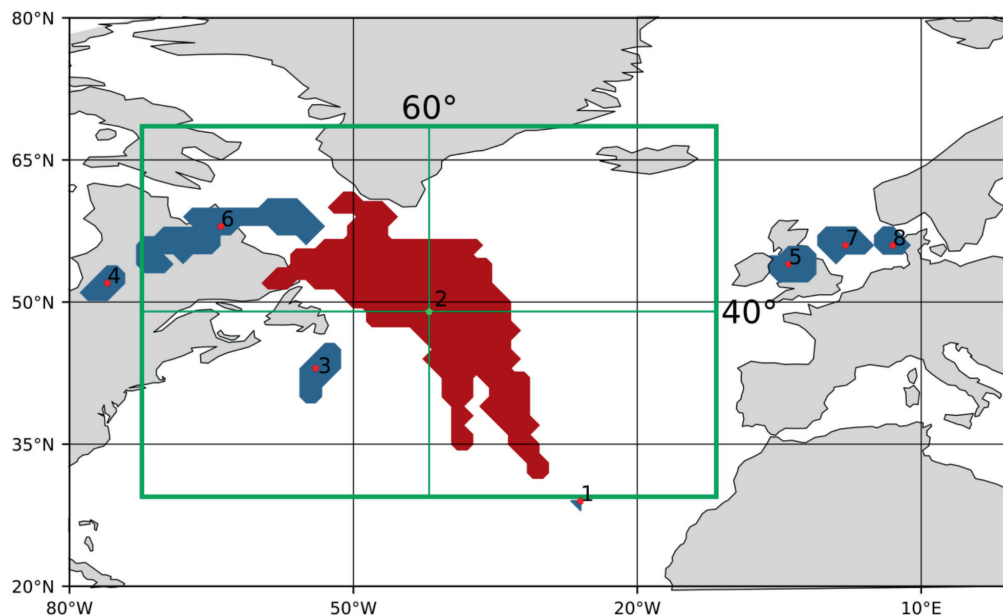
FIGURE 2 Illustration of the WCB object detection and selection, and the subsequent construction of object-centered composites. The shading shows WCB outflow objects that have been detected by the object identification algorithm in member 1 of the ECMWF ensemble forecast initialised on Jan 31 at 0000 UTC at a lead time of 90 hr. The colored dots mark the center of mass of WCB outflow objects, and numbers indicate the IDs of the individual objects. The masks with IDs 2 and 6 fulfill the size criterion ($\geq$300,000 km^2); all other masks are too small and therefore omitted. The green rectangle visualises the region centered on the outflow object with ID 2, which is extracted for the composite calculation (60° longitude, 40° latitude). [Colour figure can be viewed at wileyonlinelibrary.com]

forecast error is apparent across the northern North Atlantic, ranging from the North American east coast towards the west coast of Scandinavia (shading in Figure 3b). This pattern has similarities to climatological occurrence frequencies of extratropical cyclones (Sprenger *et al.*, 2017), often also referred to as the storm-track region. The largest errors occur in the eastern North Atlantic in the region of the climatological ridge and large $Z500$ variability, south of Iceland. WCB ascent occurs mainly from the western to the central North Atlantic, where frequencies exceed the 5% level (green contours in Figure 3b). The region of enhanced climatological $Z500$ errors is co-located with the northeastern edge of the WCB ascent region, even though a large part of the WCB ascents occurs more to the southwest, where the $Z500$ errors are rather low. The maximum WCB outflow occurrence (blue contours) is located over the central North Atlantic and extends northeastwards into the region where the $Z500$ errors are largest.

The $WS250$ climatology in the North Atlantic domain is characterised by a distinct maximum (jet) ranging from eastern North America into the central North Atlantic (shading in Figure 3c). Another maximum appears in the southeast of the plotted domain, which corresponds to the subtropical jet. The largest climatological errors of $WS250$ are shifted eastwards with respect to the maximum wind speeds and occur over the central North Atlantic and reach into western Europe (shading in Figure 3d). In that region,

the standard deviation of $WS250$ over all ensemble members and initial times (i.e., synoptic variability; contours in Figure 3c) is also large compared with other regions in the North Atlantic European domain, which indicates that the model has deficiencies in forecasting the variability of $WS250$. The region of largest $WS250$ errors is co-located with the maximum WCB outflow frequencies, which reach values above 15% in the core region of $WS250$ errors.

This shows that forecast errors and WCBs appear in similar regions, on average. In the following section, we will investigate whether WCBs are involved in the degradation of forecast skill by evaluating the temporal relationship between forecast errors and the occurrence of WCBs.

3.2 | Temporal relations between WCBs and forecast error

3.2.1 | Forecast error during periods of high and low WCB activity

The area-mean evolution of $Z500$ RMSE, averaged for the forecasts with the 20% highest (red) and 20% lowest (blue) WCB activity in the North Atlantic domain, is shown in Figure 4. Both the WCB activity and the $Z500$ RMSE are evaluated in the same region (60°W–0°E, 35°N–75°N; see white box in Figure 3). The WCB activity is computed as
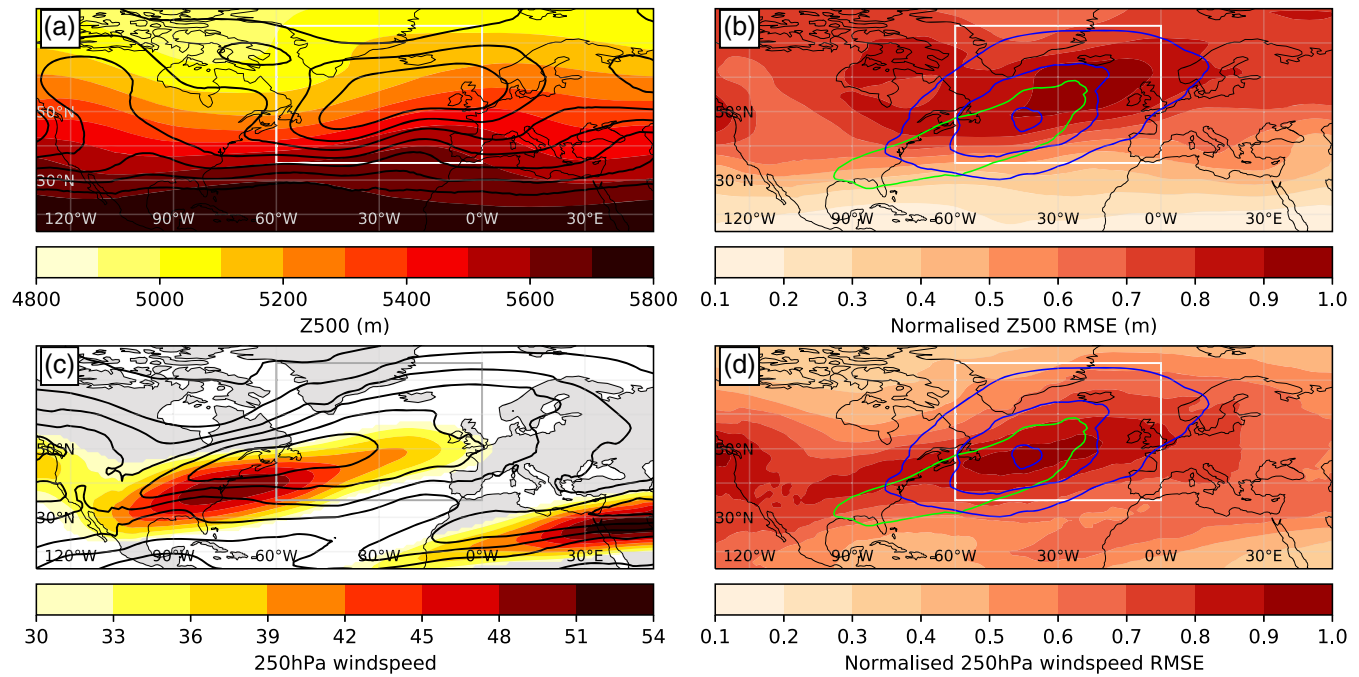
FIGURE 3 Model climatology derived from forecasts initialised in winter (DJF) 2018/2019, 2019/2020, and 2020/2021, averaged over lead times from 0–240 hr and over 50 perturbed ensemble members of (a) $Z500$ mean (shading) and normalised standard deviation (contours from 0.1–0.9 in intervals of 0.1), (b) normalised $Z500$ RMSE (shading) and WCB ascent (green contours) and outflow (blue contours) frequencies, (c) wind speed at model level 52 (approx. 250 hPa) mean (shading) and normalised standard deviation (contour lines from 0.1–0.9 in intervals of 0.1), and (d) normalised $WS250$ RMSE (shading) and WCB ascent and outflow frequencies (contours). The green and blue contours in (b) and (d) are 5%, 10%, and 15%. The RMSE and standard deviations are normalised by the maximum value within the plotting domain for each lead time. Note that the standard deviations are computed over all initial times and ensemble members, respectively. The white box shows the domain that is used for spatial averages in subsequent analyses (60°W–0°E, 35°–75°N). [Colour figure can be viewed at wileyonlinelibrary.com]

the area-mean value of the gridded WCB masks in the outflow stage of the forecasts. In Figure 4a, all lead times are considered for the classification of the forecasts into "high activity" and "low activity" groups. The general evolution of the RMSE with forecast lead time is characterised by a monotonic increase, reflecting the inevitable growth of errors during the course of the forecast. The differences of the two subgroups clearly indicate that forecasts with high WCB activity generally have less skill than forecasts with low WCB activity (e.g., RMSE of 80 m with high WCB activity and 71 m with low WCB activity on day 7). In terms of lead-time loss (i.e., the horizontal difference between the two groups at a specific RMSE level), the forecasts with high WCB activity already reach the 10-day RMSE level of the forecasts with low WCB activity after 210 hr (9 days). These results are in line with Wandel *et al.* (2021).

The subsequent panels of Figure 4 also show the average $Z500$ error for forecasts with high and low WCB activity, but with the difference that the classification is based on the WCB activity in a specified time interval of the forecasts. In Figure 4b, the WCB activity is quantified during the first two days of the forecasts. In that case, the forecast error between the two groups does not differ (except

for lead times around 8 days, which cannot be explained here). When the evaluation window is shifted to forecast days 2–4 (Figure 4c), the two subgroups show a very similar error growth behavior until the evaluation period starts (at lead times of 48 hr). Subsequently, the forecasts with high WCB activity are characterised by slightly increased values of RMSE until about day 7, after which the differences between the groups nearly vanish. The low-WCB forecasts reach the RMSE level of the high-WCB forecasts at the end of the evaluation period 6 hr later (i.e., the flow-dependent lead-time loss is 6 hr). Moving the two-day evaluation window even further results in an equivalent behaviour: when reaching the start of the evaluation period, the errors in the category with high WCB activity increase relative to the low-activity forecasts. Before that time, the lines are hardly distinguishable. The differences between the groups are largest when the WCB activity is evaluated in the intervals 96–144 hr (lead-time loss of 12 hr, Figure 4d) and 144–192 hr (lead-time loss of 18 hr, Figure 4e). For 192–240 hr (Figure 4f), the vertical differences are again smaller than in the two previous windows, even though the lead-time loss is even larger (24 hr). After the evaluation time, the RMSE of the low-WCB activity
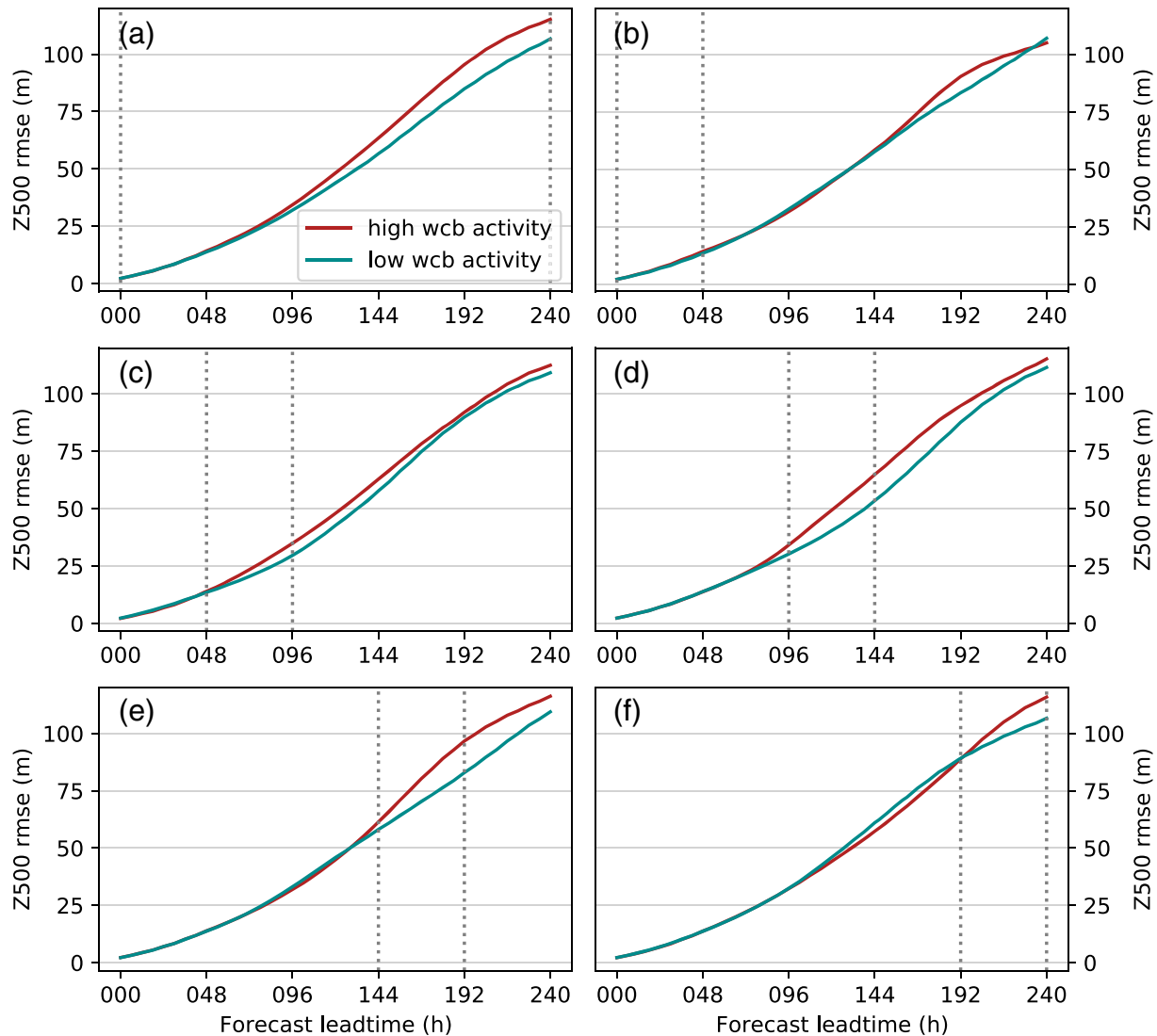
FIGURE 4   Mean evolution of root-mean squared error (RMSE) of Z500 with forecast lead time in the North Atlantic domain (60°W–0°E, 35°N–75°N) for subsets of forecasts with the 20% highest (red) and lowest (blue) amounts of WCB outflow activity at (a) all forecast lead times, and for lead times (b) 0–48 hr, (c) 48–96 hr, (d) 96–144 hr, (e) 144–192 hr, and (f) 192–240 hr. The dotted gray lines mark the evaluation period of WCB activity. [Colour figure can be viewed at wileyonlinelibrary.com]

forecasts slowly reaches the RMSE of forecasts with high WCB activity (all panels of Figure 4 except a and f).

This analysis shows that the occurrence of forecast errors and WCBs are related in time and therefore suggests that WCBs on average might dilute the forecast performance. Under the hypothetical assumption that both subgroups (i.e., low and high WCB activity) are characterised by similar dry dynamic activity, these results would imply that error growth is larger in situations with moist baroclinic contributions reflected in WCB activity compared with flow configurations mostly governed by dry dynamics. The impact of WCB activity is weaker when the WCB occurs in an early stage of a forecast, suggesting that a previously existing error source is favorable for the subsequent error growth due to WCBs. The lead-time

loss increases steadily when the WCB activity is evaluated at later lead times, as it becomes more likely that forecast errors have already emerged which can be propagated or amplified by WCBs. At lead times beyond the ones analysed in this study (i.e., longer than 10 days), the impact will most likely decrease, as the growth rate levels off (this can be seen already in the blue line of Figure 4f) and the forecast errors start to saturate.

3.2.2 | Focus on time of maximum error growth

Even though it was shown that anomalous WCB activity co-occurs with reduced forecast skill, this does not imply

that the error growth is induced by WCBs. To elaborate further on a potential causal relationship, we now focus on the time in the forecast during which the error grows fastest. To do so, the slope of the area-averaged evolution of $Z500$ RMSE of all individual forecasts is computed, and the RMSE as well as the WCB activity within the same region is lagged on that lead time at which the absolute RMSE growth is largest. We choose the absolute error growth over the relative error growth, as the latter strongly emphasises very early lead times at which random errors grow mainly on the convective scale (e.g., Zhang *et al.*, 2007). Only lead times up to 192 hr are considered to ensure the availability of data at time lags up to 2 days after the maximum RMSE growth occurred. Note that all forecasts are considered, not only bad or good ones.

Typically, the maximum error growth of $Z500$ in the North Atlantic occurs between days 5 and 7 of the forecast, with the median of the distribution at a lead time of 150 hr (Figure 5a). However, some forecasts experience their strongest degradation at earlier times: 5% of the forecasts have the strongest forecast error growth before day 4.

The mean evolution of the area-averaged RMSE is characterised by a constant, but slow increase 72–12 hr before the time of maximum error growth (blue line in Figure 5b). By definition, the RMSE grows rapidly around time lag 0, while its slope flattens out after time lags larger than 12–18 hr. The reason for this saturation is that these time lags correspond mainly to lead times larger than 8 days, during which the Rossby-wave patterns in the forecast and analysis start to become out of phase and errors begin to saturate (e.g. Baumgart *et al.*, 2019).

Around the time of maximum error growth in each individual forecast, the area-averaged WCB activity is systematically increased (red lines in Figure 5). On average, the WCB inflow frequency anomaly (dashed line) reaches its maximum of 10% 12 hr prior to the strongest increase of forecast error, but already starts to be above the climatological mean about 1–2 days before. 18–24 hr after the maximum RMSE growth rate, the WCB inflow occurrence drops below climatological occurrence frequencies. WCB ascent and outflow anomalies evolve almost simultaneously and show a similar pattern to the inflow, but shifted towards later time lags: values start to be higher than the model climatology 18 hr before and reach their maximum of about 12% on average 6–18 hr after the forecasts experience their strongest degradation.

The synoptic evolution around the time of maximum error growth is depicted in Figure 6. Originating from a situation with a slightly amplified flow configuration 2 days prior to the largest increase of $Z500$ RMSE (Figure 6a), the Rossby-wave pattern is amplified further (Figure 6b–d) and reaches its maximum stage on the day of maximum error growth (Figure 6e), with a wave pattern extending from the North American east coast towards northern Europe. Ahead of a trough emerging from continental North America, higher-than-usual WCB outflow (2%–3%, absolute anomalies) is directed into the central North Atlantic and builds up a ridge. Prior to the maximum forecast error growth in the North Atlantic, the upstream trough is mainly associated with anomalous forecast errors (red contours in Figure 6d), which grow further (Figure 6e) and are finally distributed across the North Atlantic by
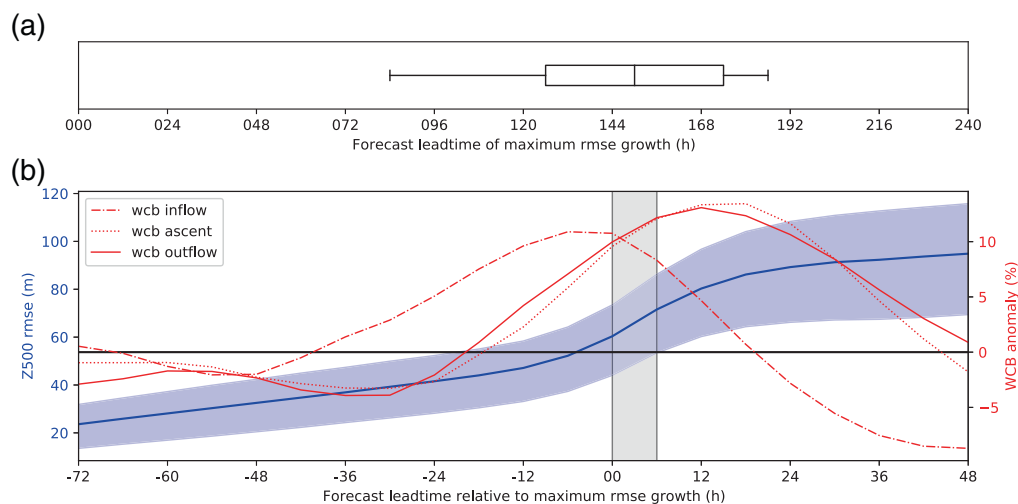

FIGURE 5 (a) Distribution (box indicates the interquartile range, whiskers the 5–95 interquantile range) of forecast lead times when the maximum error growth occurs in the North Atlantic region (60°W–0°E, 35°N–75°N). (b) Mean (blue line) and interquartile range (blue shading) of the evolution of the domain-integrated $Z500$ RMSE and the domain-integrated relative WCB anomaly (i.e., absolute anomaly divided by climatological mean: dash–dotted: inflow; dotted: ascent; solid: outflow) lagged on the lead time of maximum error growth in the North Atlantic region. The gray bar highlights the section with the largest error growth between two time steps. [Colour figure can be viewed at wileyonlinelibrary.com]
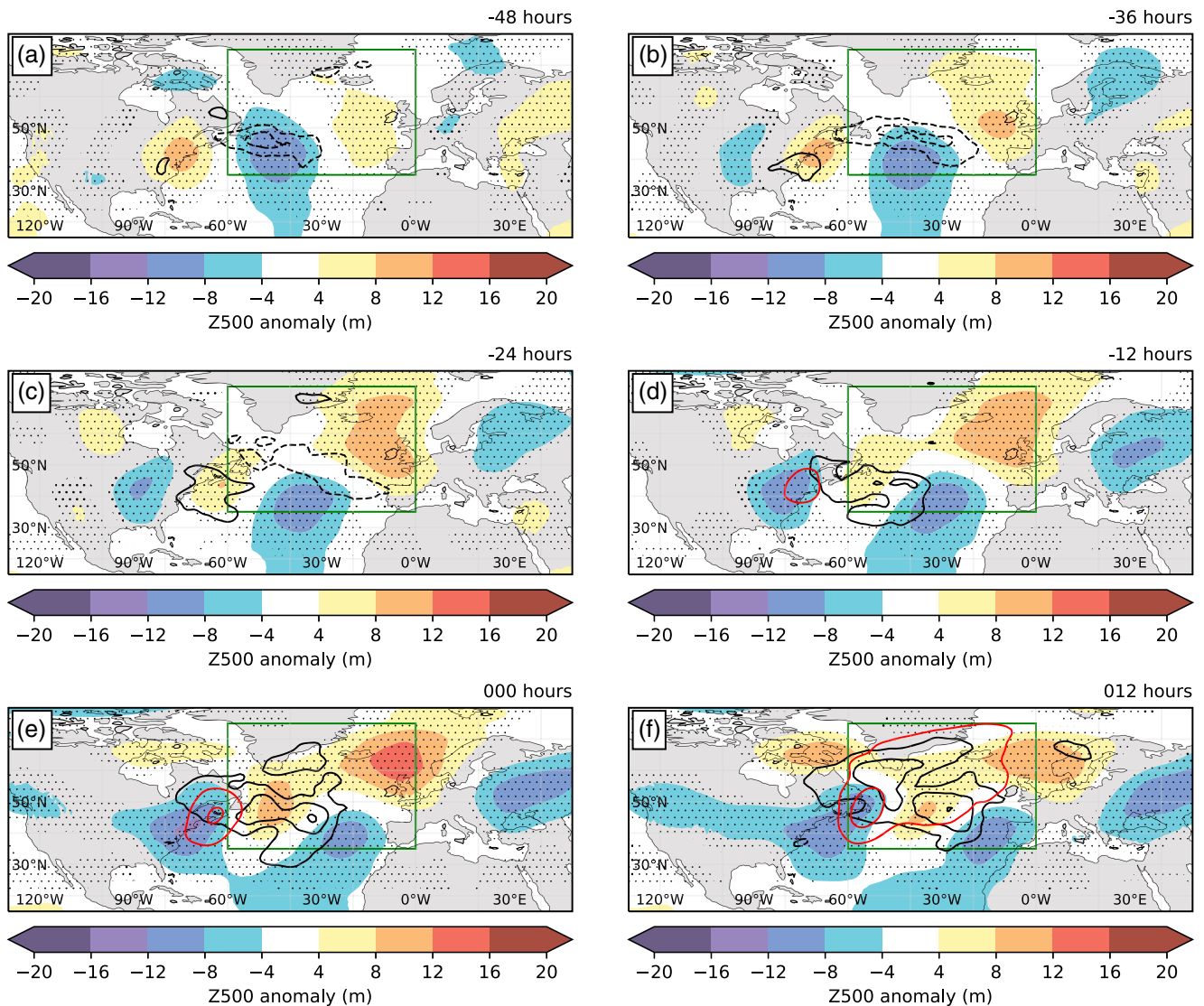
FIGURE 6 Composites of *Z500* anomalies relative to model climatology (shading) and absolute WCB outflow frequency anomalies (solid black contours of 1%, 2%, and 3%, dashed black contours of −1%, −2%, and −3%) and *Z500* RMSE anomalies (red contours from 10–30 m in 10-m intervals) with time lags of (a) −48 hr, (b) −36 hr, (c) −24 hr, (d) −12 hr, (e) 0 hr, and (f) 12 hr to the maximum error growth in the North Atlantic region (60°W–0°E, 35°N–75°N) outlined by the green box. The stippling shows *Z500* anomalies that are statistically significant at a confidence level of 0.99 based on a two-sided *t*-test. [Colour figure can be viewed at wileyonlinelibrary.com]

WCB outflow (Figure 6f). Overall, the magnitudes of both the *Z500* and WCB anomalies are rather small. However, it has to be taken into account that no classification into subgroups has been done (i.e., good versus bad forecasts) and very different synoptic situations are included in the composites. Despite this circumstance, the analysis shows that forecast skill deterioration over the North Atlantic on average coincides with enhanced WCB activity and upper-level ridge building.

A sharper picture emerges when the same analysis is carried out with forecasts classified into "good" and "bad" groups. In doing so, the 20% forecasts with the largest spatio-temporal RMSE averaged over forecast times

0–240 hr are labelled as "bad", while the 20% forecasts with the lowest RMSE are classified as "good". The slope of the RMSE curve lagged on the maximum error growth is much steeper for the bad forecasts (dashed blue lines in Figure 7) than for the good forecasts (dotted blue lines in Figure 7), resulting in much larger RMSE values at the end of the time series. The WCB activity (only outflow shown) is also fairly different in the two subsets: the bad forecasts (red line) are already characterised by a high level of WCB outflow frequency 3 days prior to the maximum error growth. At time lag −24 hr, the WCB anomalies increase to even larger values and reach their maximum of more than 20% around 12 hr after the strongest error
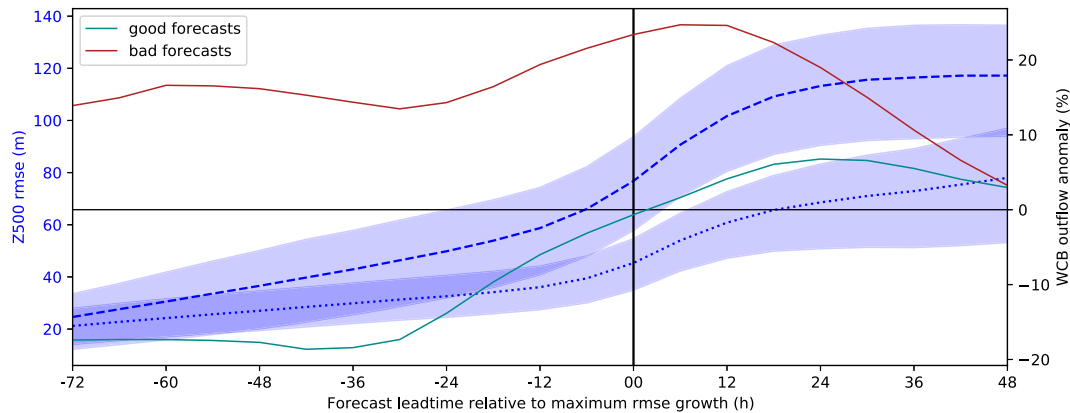
FIGURE 7   As Figure 5, but for WCB outflow only and for the 20% best forecasts (blue dotted line: RMSE, green line: WCB outflow activity) and the 20% worst forecasts (blue dashed line: RMSE, red line: WCB outflow activity). [Colour figure can be viewed at wileyonlinelibrary.com]

growth occurred. Subsequently, the values decrease and approach climatological mean values. The forecasts with low RMSE values, in contrast, have a generally much lower level of WCB activity (blue line). At time lags −72 to −24 hr, the area-averaged outflow anomalies are just above −20%. When approaching the time of strongest error growth, however, the WCB frequency also increases in the group of good forecasts and reaches its maximum of about 5% at time lag 24 hr. Hence, not only do bad forecasts worsen in this moist baroclinic environment, but also good ones.

The synoptic situations of the two subgroups differ substantially (Figure 8; note the different contour levels/shading compared with Figure 6): the "good" forecasts (Figure 8a,c,e) are characterised by a strong cyclonic anomaly over the whole North Atlantic, which splits up into eastern and western parts during the maximum error growth. Along the leading edge of the trough in the western North Atlantic, WCB outflow is directed into the central North Atlantic, where it weakens the cyclonic anomaly. In contrast, the "bad" forecasts are dominated by a distinct anticyclonic anomaly that is located over the northeastern North Atlantic (Figure 8b,d,f). This persistent anomaly is constantly fed by anomalously frequent WCB outflow, also prior to time lag −36 hr (not shown). Moving closer to the maximum error growth, the anticyclonic anomaly intensifies and expands towards the central North Atlantic, as an upstream positive $Z500$-anomaly, which is co-located with enhanced WCB outflow frequency, merges into the main anomaly (Figure 8f). Similar to the full composite (see Figure 6), this WCB event amplifies forecast errors that are associated with the upstream trough and spreads them across the North Atlantic. Despite larger-than-usual WCB activity in the western North Atlantic in the "good" forecasts (Figure 8c,e), the error does not grow at the same rate as

in the "bad" forecasts. This is a strong indication that situations with enhanced WCB activity efficiently amplify pre-existing errors (as in the "bad" forecasts) but are not necessarily a source of error when little or no pre-existing error is present (as in the "good" forecasts). Thus, when upstream forecast uncertainty is small, WCBs are much less efficient in amplifying forecast error and projecting it downstream.

A very similar pattern is evident when the forecast error is not evaluated in the North Atlantic domain, but further downstream over Europe. Prior to the maximum error growth rate, the WCB activity is systematically increased in the upstream region (see Figure S3 in the Supporting Information). Compared with the in situ perspective, the maximum WCB occurrence in the upstream box occurs one day earlier, which reflects the propagation of the signal with the background winds. The large-scale flow configuration around the time of maximum forecast degradation over Europe resembles the one from the North Atlantic region, as it is characterised by a positive geopotential anomaly and by anomalously high WCB outflow frequencies over Europe (see Figure S4 in the Supporting Information). Again, higher-than-usual $Z500$ RMSE associated with an upstream cyclonic anomaly is amplified and propagated into the ridge by anomalous WCB activity. Also, the classification into "good" and "bad" forecasts over Europe results in two distinct flow configurations. Consistent with the results of Büeler et al. (2021), the good forecasts feature a NAO−/Greenland blocking pattern, whereas the bad forecasts are characterised by a European blocking pattern (see Figure S5 in the Supporting Information).

This analysis shows that the occurrence of WCBs is systematically increased around the time of the strongest reduction of forecast skill, and that WCBs amplify and
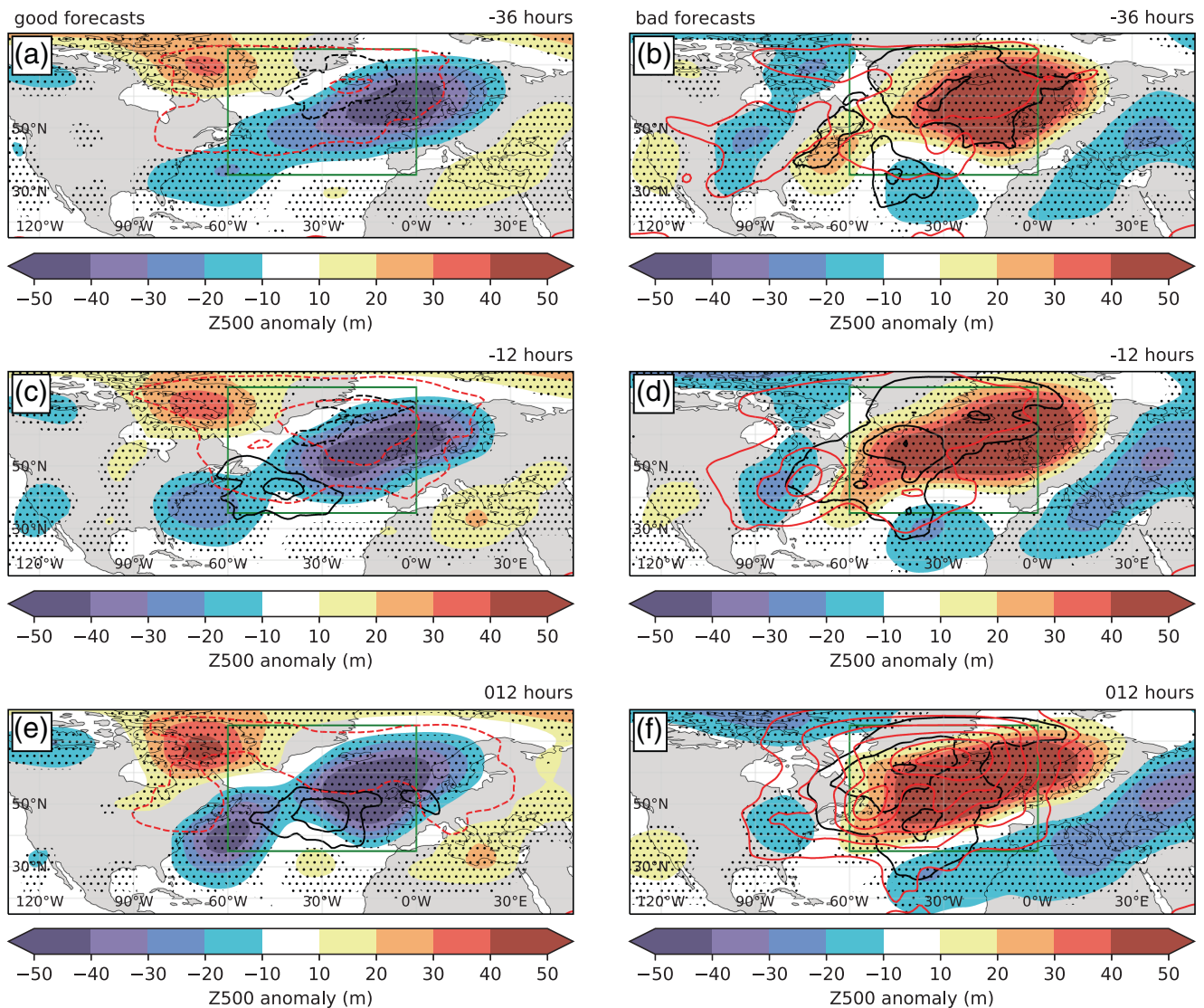
FIGURE 8   As Figure 6, but separated for the 20% best (a,c,e) and 20% worst forecasts (b,d,f) and only for time lags (a,b) −36 hr, (c,d) −12 hr, and (e,f) 12 hr. WCB outflow anomalies are shown as solid black contours from 2.5%–10% in 2.5% intervals and as dashed black contours from −2.5% to −10% in 2.5% intervals. Solid red contours show positive Z500 RMSE anomalies from 10–100 m in 10-m intervals, dashed red contours show negative anomalies from −10 to −100 m in 10-m intervals. The stippling shows Z500 anomalies that are statistically significant at a confidence level of 0.99 based on a two-sided t-test. [Colour figure can be viewed at wileyonlinelibrary.com]

redistribute pre-existing forecast errors associated with cyclonic flow anomalies. This is particularly the case for forecasts of poor quality, where WCB frequencies are generally increased. In comparison with the "bad" forecasts, the "good" forecasts are characterised predominantly by strong cyclonic anomalies associated with a lack of WCB activity and upper-level ridge building. This flow configuration is associated with an eastward extension of the jet (Figure S6a,c,e in the Supporting Information), which strongly resembles the "central jet" configuration defined in Madonna *et al.* (2019, see their Figure 3). The composite of the "bad" forecasts, in contrast, resembles the "mixed jet" configuration, in which the jet is retracted and

deflected poleward (Figure S6b,d,f in the Supporting Information). Madonna *et al.* (2019) show that both jet configurations are characterised by similar values of eddy kinetic energy, and thus provide equally favorable conditions for baroclinic growth. Hence, one could expect similar error growth due to dry dynamic processes in the two subsets. Nevertheless, the forecast error is substantially smaller in the composite of the "good" forecasts than in the other subset, where the WCB frequency is much higher. Similarly to the analysis in Section 3.2, this suggests that WCBs play an important role for forecast error growth and should not be considered as a byproduct of cyclone activity. These results are in line with the findings of Rodwell *et al.* (2013),

who found that situations of low predictability over Europe are often associated with atmospheric blocking, and stated that diabatic processes might play an important role for the degradation of the forecasts.

3.3 | Perspective on WCB objects

So far, the analysis has focused on composites anchored on the time of maximum forecast error growth in a large, predefined domain, which makes it difficult to establish a causal relationship between WCBs and forecast error growth, as other processes that occur simultaneously could also be involved. To elaborate further on a possible causality, we adopt one further perspective that focuses on WCB objects in the forecasts by computing WCB-centered composites of meteorological variables and error metrics (see Section 2.4 for a detailed description of the methodology).

3.3.1 | Meteorological composites

Figure 9 shows composites of $Z500$ anomalies (shading), MSLP anomalies (black contours), and $WS250$ anomalies (purple contours) centered on WCB outflow objects at time lag 0 hr for time lags three days prior until three days after the detection of WCB outflow objects. For clarity, no WCB frequencies are shown in this figure. It is, however, important to note that WCB frequencies (especially of the outflow phase) have already appeared before the actual time of detection (i.e., lag 0 hr, Figure 9d) because WCB objects typically last a few days. This can be seen later in Figures 10 and 11. The composites are averages over WCB outflow objects that appear during forecast lead times 72–168 hr centered on lag 0 hr, which ensures full data coverage at all time lags, and each panel is a temporal average over four time steps with six-hourly increments (e.g., −3 to −2 days lag is the average over 72–54 hr prior to the outflow event).
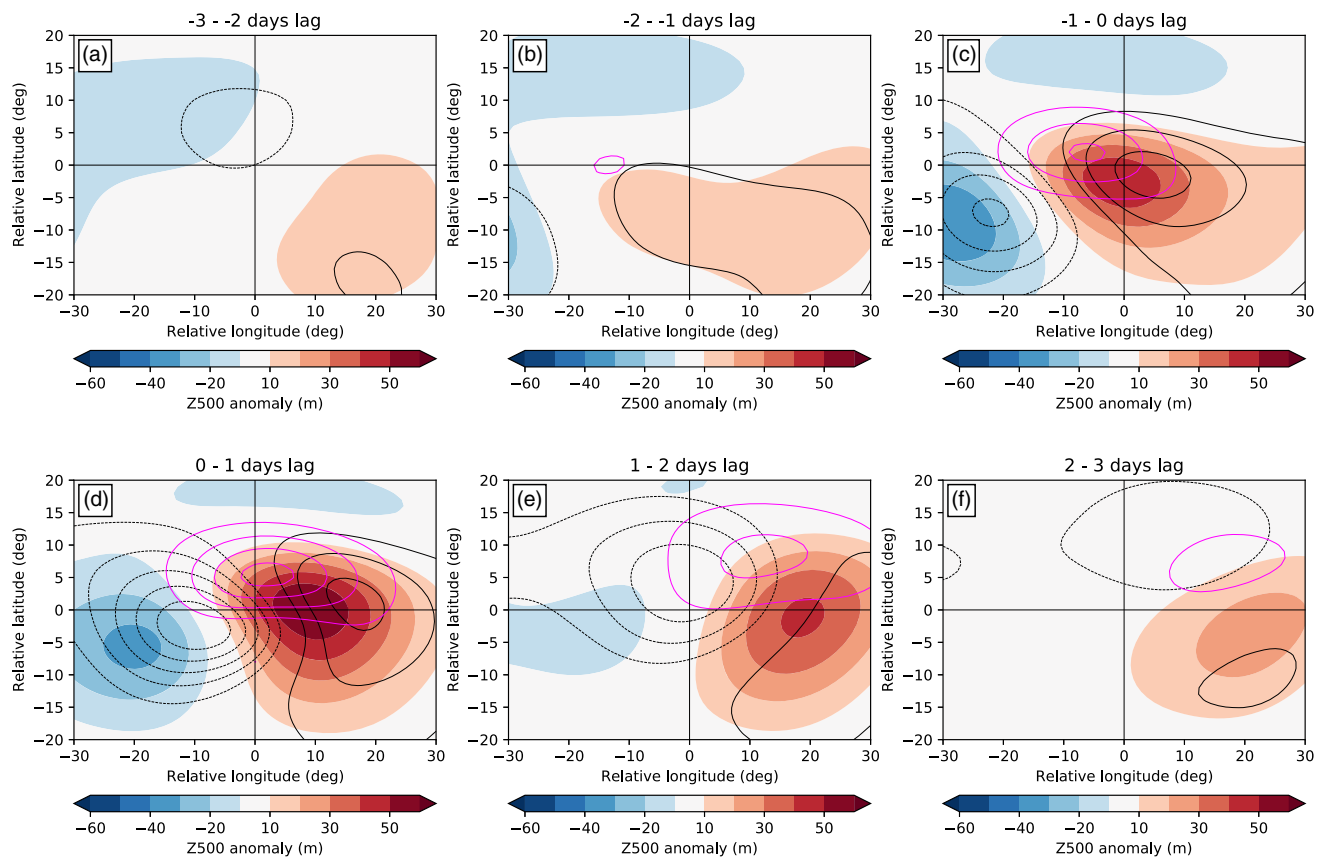

FIGURE 9 Composite means of $Z500$ (shading), MSLP (black contours from −10 to 10 hPa in 1 hPa steps), and $WS250$ (pink contours at 3, 6, 9, and 12 m·s^{-1}) anomalies centered on WCB outflow objects. Anomalies are differences of the instantaneous field and the model climatology at the corresponding grid points. The spatial composites are means over the forecast lead times 72–168 hr (17 forecast lead times). Shown are temporal means over (a) 3–2 days (72–54 hr) before, (b) 2–1 days (48–30 hr) before, (c) 1–0 days (24–6 hr) before, (d) 0–1 days (0–18 hr after), (e) 1–2 days (24–42 hr) after, and (f) 2–3 days (48–66 hr) after the WCB outflow event. The number of composite members is 541,033. [Colour figure can be viewed at wileyonlinelibrary.com]

At lags three to two days prior to the evaluation time (Figure 9a), the Z500 field is close to the climatology, with a slight tendency for a positive anomaly indicative of a downstream ridge in the southeastern quadrant and a negative anomaly indicative of a trough in the northwestern quadrant, both accompanied by a corresponding MSLP anomaly. Two to one days prior to the detected outflow event (Figure 9b), the upstream anomaly intensifies indicating an approaching trough, and a weak signal of enhanced wind speed emerges upstream of the composite center. On lag days −1 to 1 (Figure 9c,d), both the anomalies related to the downstream ridge and the upstream trough as well as the MSLP anomalies intensify further, the anomalies exhibit a westward tilt with height indicating a baroclinic development, and the WS250 anomaly located north of the composite center is maximised on the day of the WCB detection. One to two days after the event (Figure 9e), the downstream ridge and the wind speed anomaly are still pronounced, and the upstream signal is only present as negative MSLP anomaly but nearly vanishes in the mid-troposphere. One day later, the anomalies have weakened considerably and the fields are again close to climatology (Figure 9f). The synoptic sequence of ridge building and amplification and the formation of a WS250 anomaly related to a jet streak associated with WCB outflow events is well understood (see e.g., Grams and Archambault, 2016) and matches the previously shown composites of Z500 around the time of maximum forecast error growth (see Figure 6). A similar sequence is apparent when the composites are centered on the ascent phase of WCBs. The pattern, however, is shifted northeastward, as the WCB ascent typically occurs slightly upstream of the outflow (not shown).

3.3.2 | Error composites

We here show similar composites, but now for the normalised RMSE in the mid troposphere (Z500) and upper troposphere (WS250). As the ascent phase of WCBs occurs in the mid troposphere, the Z500 errors are centered and lagged on WCB ascent objects (Figure 10). For further guidance, the WCB inflow (orange contours), ascent (green contours), and outflow (blue contours) frequencies relative to the ascent event are plotted. Three to two days prior to a WCB ascent event, the RMSE in the region is similar to the climatological forecast error (Figure 10a). Two to one days before the event (Figure 10b), increased errors (15%–20% larger than climatological errors) emerge in the southwestern quadrant of the composite, upstream of anomalous WCB inflow. On the two days around the WCB ascent event (Figure 10c,d), the error pattern amplifies further (> 30%) and propagates eastwards; simultaneously,

WCB ascent and outflow reach their highest frequencies, with the ascent located slightly upstream of the outflow. One to two days after the WCB ascent occurred (Figure 10e), the error structure weakens and takes on an elongated shape reaching far into the northeastern quadrant, where some WCB outflow is still present. On days 2–3 (Figure 10f), the magnitude of the errors decreases further and no clear structures are apparent.

The increased errors upstream of the ascent are co-located with the approaching trough in the Z500 field (compare Figures 9b,c and 10b,c), which indicates that errors are already present before the WCB event. On the two days around the WCB ascent (Figure 10c,d), large errors are associated with the maximum occurrence frequencies of ascents, indicating the likely amplification of pre-existing error by the diabatic processes in the ascending air stream. The downstream errors in the region of the WCB outflow are associated with the jet intensification and ridge building in the northeastern quadrant (note the meridional shift between the ascent and outflow phase). Interestingly, this region is not associated with above-normal errors before the WCB event occurs, which points towards the propagation and/or amplification of forecast errors from the trough into the ridge by WCBs.

Despite the clear error patterns related to the upstream trough and the (downstream) ridge, the variability among the composite members is very large: an investigation of the individual composite members with a k-means clustering algorithm (Hartigan and Wong, 1979) shows that about 50% of the cases are characterised by errors that are similar to or even smaller than the climatological mean (not shown). The other half of the composite members are subject to substantial case-to-case variability. This reflects that the structure of the mid-tropospheric error patterns in the vicinity of WCBs is rather complex and cannot be entirely attributed to the WCB itself, but is also affected by Rossby-wave dynamics.

Next, composites of the relative RMSE of 250-hPa wind speed centered on WCB outflow events are analysed (Figure 11). In contrast to the mid-tropospheric errors, no upstream errors are apparent for the upper-level wind speed. Errors first become visible about 2 days before the WCB outflow occurs west of the composite center (Figure 11b), propagate eastwards and intensify to maximum values of more than 30% on lag day 0–1 (Figure 11d). The elliptic shape of the error pattern strongly resembles the shape of the jet streak that accompanies the WCB outflow and is located north of the main WCB outflow and at the northwestern edge of the developing ridge. By lags day 1–3 (Figure 11e,f), downstream errors also emerge in the upper-level wind field. These errors could be related to anticyclonic breaking of the downstream ridge or to downstream development of a trough. In contrast to the
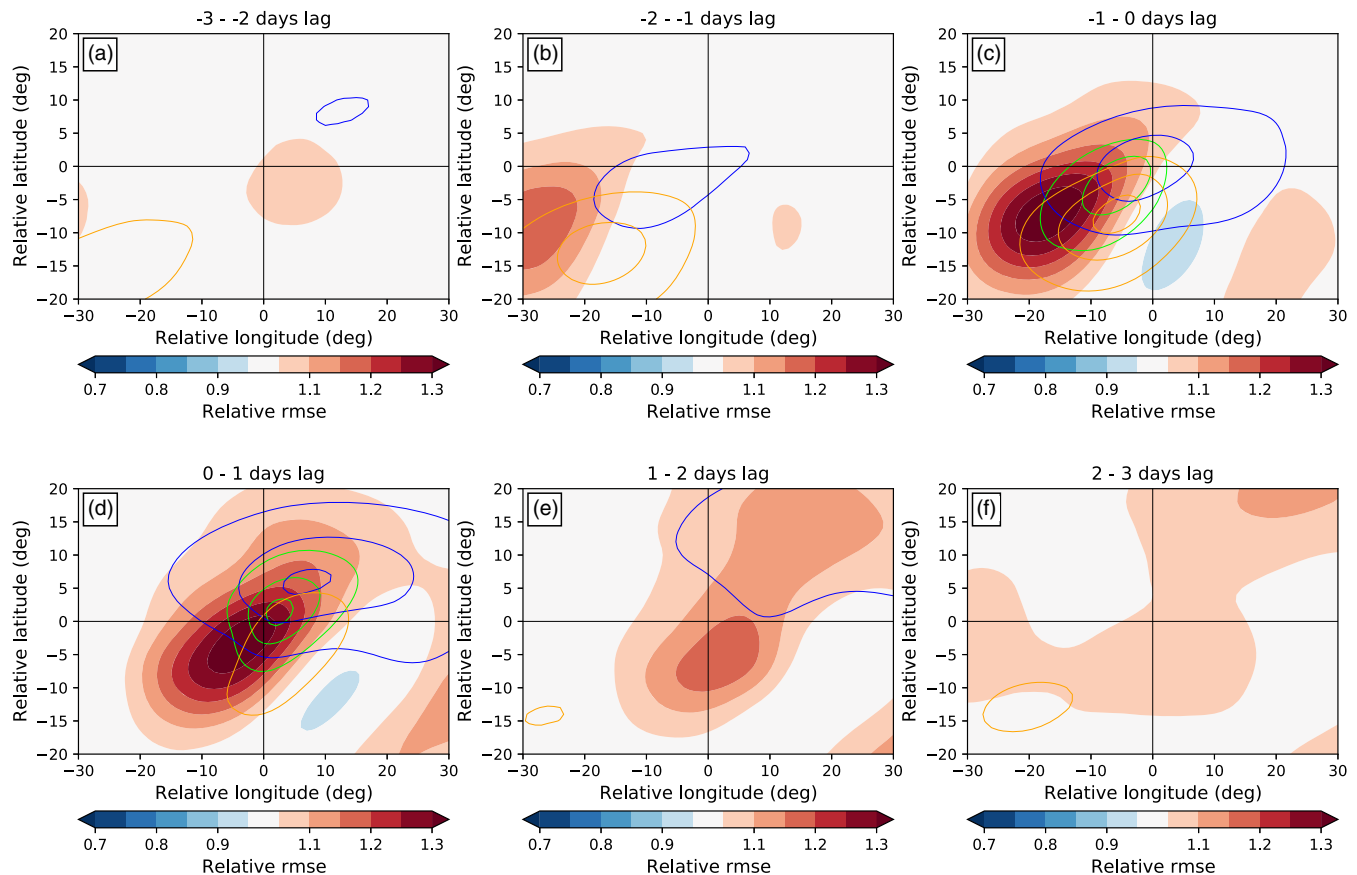
FIGURE 10 As Figure 9, but centered on objects of WCB ascent and for the RMSE of $Z500$ normalised by the climatological RMSE (shading; a value of 1.1 indicates an error that is 10% larger than the climatological error). Colored contours show frequencies of WCB inflow (orange), ascent (green), and outflow (blue) at levels of 12.5%, 25%, and 37.5%. The number of composite members is 316,769. [Colour figure can be viewed at wileyonlinelibrary.com]

mid-tropospheric errors, the individual composite members of $WS250$ errors are mostly characterised by spatially coherent error patterns, and the largest part of the cases are associated with above-climatological errors.

A qualitatively similar picture emerges when the variables for the composites centered on the WCB stages are swapped (i.e., $Z500$ errors centered on WCB outflow or $WS250$ errors centered on WCB ascent), when the spatial displacement of the WCB ascent relative to the outflow is considered. The spatial variability of mid-tropospheric errors persists even when centered on the outflow, and the error patterns of the upper-level wind speed remain spatially homogeneous when centered on the ascent (not shown). This consistent response of forecast errors across the two WCB stages and variables suggests that pre-existing errors in the mid-troposphere are taken up by the WCB and projected on the upper-level flow. Thus the WCB acts primarily to amplify errors and propagates them to the upper levels.

To explore further the hypotheses on whether WCBs are a source of error or amplify pre-existing errors, we

stratify the error composites by large or small errors upstream and before the WCB event. More specifically, we select the 20% cases where the spatially and temporally integrated normalised $Z500$ RMSE in the object-relative box between 30°W–5°W, 20°S–0°N 36–12 hr prior to the WCB outflow event is smallest (i.e., small upstream error) and largest (i.e., large upstream error). This selection focuses on errors associated with the upstream trough, as for example shown in Figure 10. We are showing the error composites centered on WCB outflow events for both $Z500$ and $WS250$ RMSE, as this allows us to consider the same events for the two variables, which would not be possible when combining ascent and outflow events. For both groups (i.e., small and large upstream error), the evolution of the relative RMSE centered and lagged on the WCB outflow event is shown in Figure 12. Note that only outflow objects that occur at forecast lead time 96 hr are considered here. By design, the $Z500$ error composites for the cases with the smallest upstream error are characterised by large negative values in the southwestern quadrant upstream of the WCB event (row a). At lags after
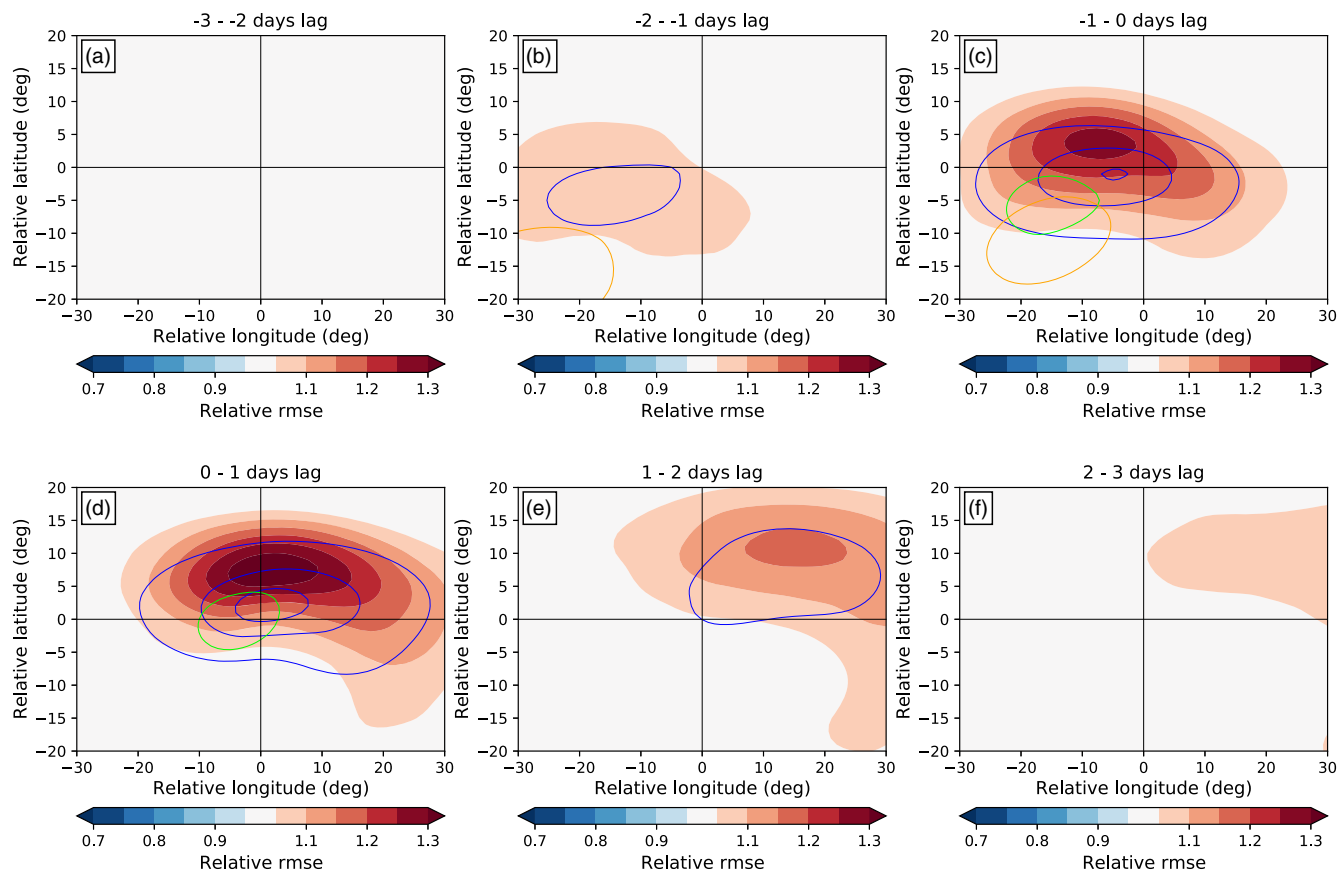
FIGURE 11 As Figure 10, but centered on objects of WCB outflow and for the RMSE of $WS250$ normalised by the climatological RMSE (shading). The number of composite members is 541,033. [Colour figure can be viewed at wileyonlinelibrary.com]

the WCB event occurred (columns 3–6), the errors are still slightly below the climatology. At upper levels (row b), the errors 3–1 days prior to the WCB outflow event are also smaller than the climatology. During maximum WCB activity (one day prior to two days after the event, columns 3–5), however, errors are larger than the climatology in the region where WCB outflow occurs. On lag day 3 (column 6), the composite reaches climatological values.

The 20% of events with highest upstream errors, in contrast, are overall characterised by above-climatological errors for both $Z500$ (row c) and $WS250$ (row d). The $Z500$ RMSE is maximised during the period 2 days prior to 1 day after the WCB outflow occurs (columns 2–4), and the error is then projected into the northeastern quadrant (columns 5 and 6). A similar evolution occurs for $WS250$, where the maximum RMSE occurs at lag zero to one days and exceeds the climatological value by more than 50%.

This analysis suggests that both error introduction and error amplification happens during WCB activity: the cases with small upstream errors in the $Z500$ field are characterised by a distinct pattern of enhanced errors in the region of WCB outflow. Hence, situations with WCB activity can produce errors at the wave guide even if the upstream trough is represented comparably well in the

forecast (note that this does not mean that there is no upstream error). Nevertheless, the errors in the region of WCB outflow are much larger and more persistent when the upstream trough is misrepresented in the forecasts, which shows that pre-existing errors are amplified by WCBs.

3.3.3 | Lead-time dependence of error composites

The previously shown error composites centered on WCB ascent and outflow objects (Figures 10 and 11) are averages over forecast lead times ranging from 3–7 days. However, it was shown in Section 3.2 that the error differences between forecasts with high and low WCB activity depend on the time when the WCB activity is evaluated (see Figure 4). To investigate this lead-time dependence of WCB-related errors further, the temporal evolution of the spatial averages of the $Z500$ and $WS250$ RMSE composites centered on WCB ascent and outflow are computed for different lead times when the WCB object is detected (Figure 13). While both variables follow a similar temporal evolution at all lead times, with maximum mean errors
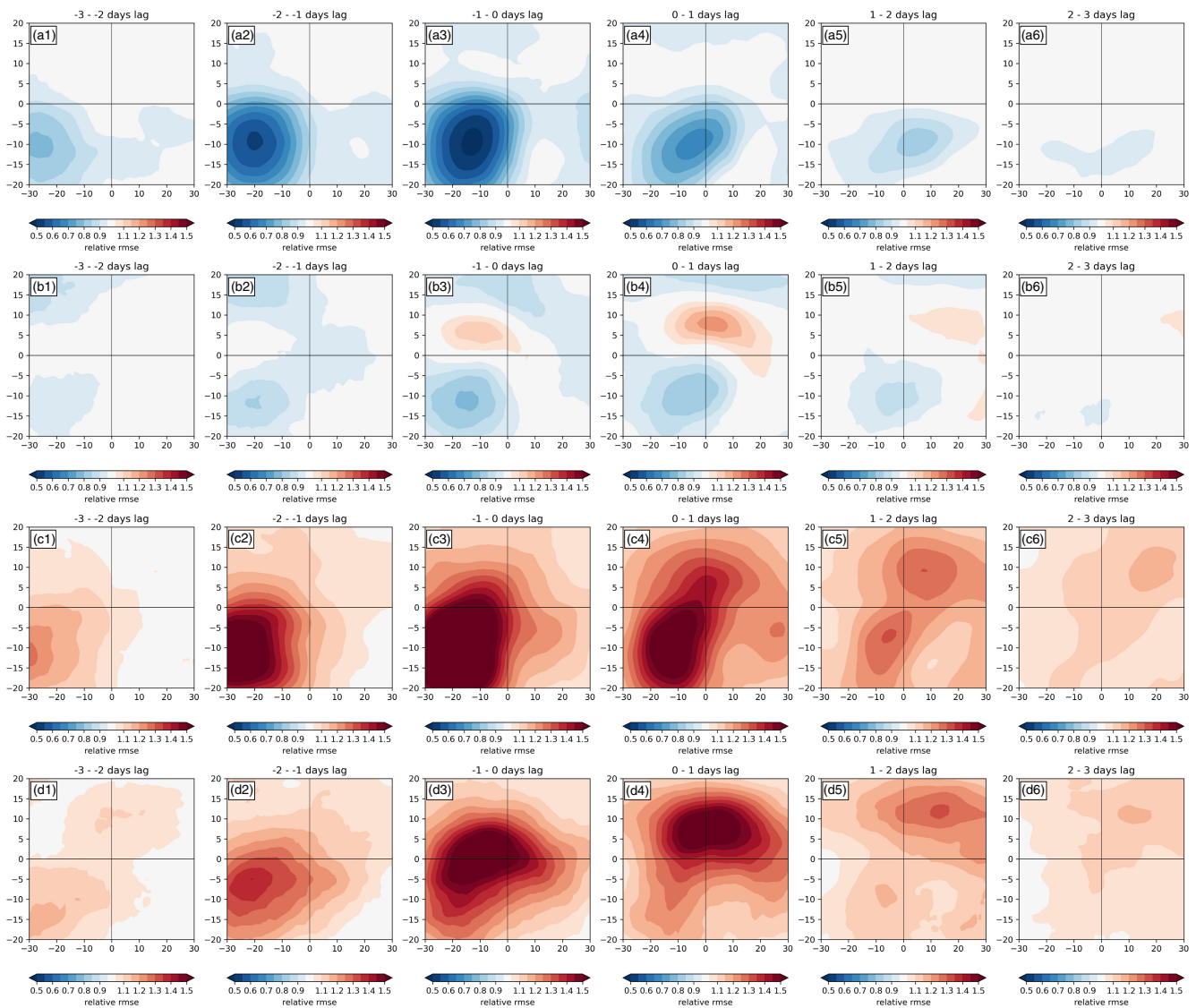
FIGURE 12 Error composites centered on WCB outflow objects for cases selected by the magnitude of normalised $Z500$ RMSE in the box 30°W–5°W, 20°S–0°N 36–12 hr prior to WCB outflow events occurring at lead time 96 hr. The top row (a) shows the composite mean of normalised $Z500$ RMSE for the 20% of cases with lowest upstream error, and the second row (b) shows the corresponding composite mean for normalised $WS250$ RMSE. The third (c) and fourth rows (d) show the same composites as the first and second rows, but for the 20% of cases with highest upstream error. The columns show time lags from 3–2 days prior to the outflow event (column 1) until 2–3 days after the outflow event (column 6). [Colour figure can be viewed at wileyonlinelibrary.com]

slightly after the WCB event, there are some differences between the mid-tropospheric and upper-level errors: the relative $Z500$ errors are on average smaller when the event occurs early in the forecast (pale colors in Figure 13a), increase for forecast days 3–5, and again decrease for late lead times (dark colors). This is substantially different from the signal observed for the upper-level wind speed errors (Figure 13b), which are largest when the WCB event occurs within the first 42 hr after the initialisation (pale colors), and subsequently decrease continuously (dark colors). Despite the larger peak of the $WS250$ RMSE at the time of the WCB event, the domain-integrated $Z500$ errors

remain at a higher level after the WCB ascent event. Except for the earliest lead times, the normalised errors are higher after the WCB event than before, which shows that the forecast skill is permanently reduced after a WCB event occurred. Hence, WCBs can be viewed as predictability barriers (Sánchez *et al.*, 2020). However, it is important to note that the evaluation domain does not move with the object, for which reason enhanced errors that are advected outside the domain are not considered here.

The larger magnitude of mid-tropospheric errors related to WCB ascents that occur at later forecast stages compared with early WCBs is in line with the analysis of

FIGURE 13 Time-lagged evolution of domain-integrated composites of the relative RMSE of (a) $Z500$ centered on WCB ascents (see Figure 10) and (b) $WS250$ centered on WCB outflow (see Figure 11). Different color shades denote the forecast lead time at which the WCB event occurs ("0d" corresponds to the average of 0, 6 12, and 18 hr, "1d" to 24, 30, 36, and 42 hr, etc.). [Colour figure can be viewed at wileyonlinelibrary.com]
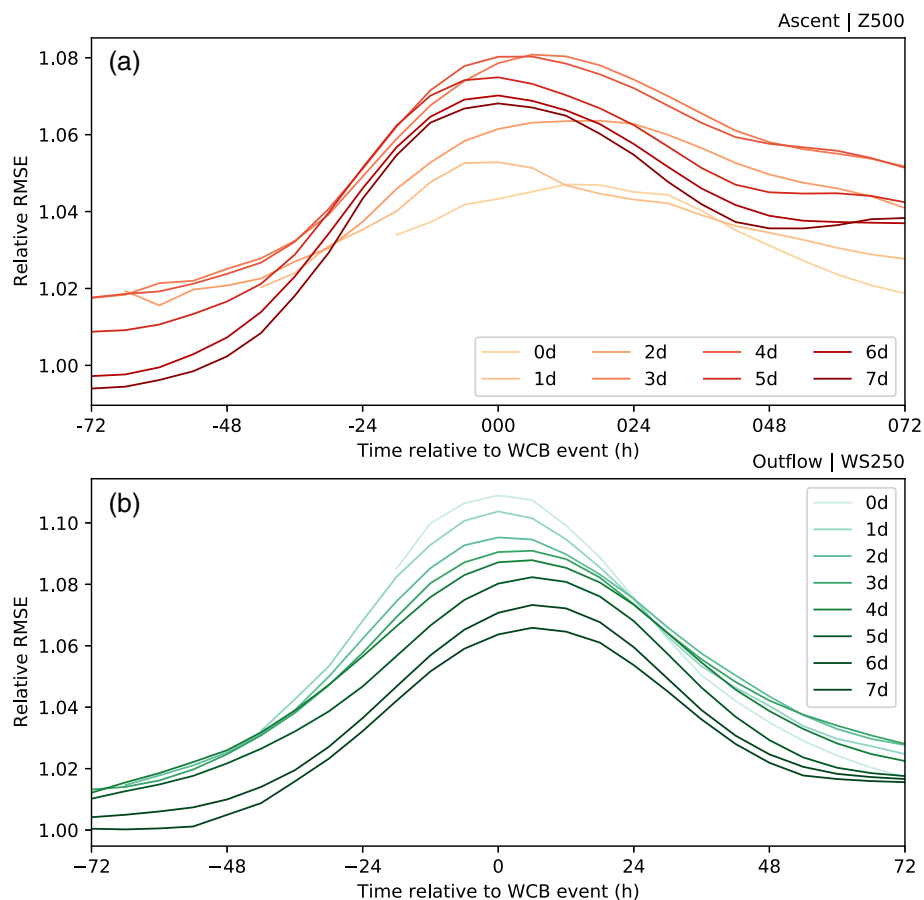
the skill of forecasts with high WCB activity at different lead times (Figure 4). This indicates that WCBs amplify and propagate pre-existing errors. On the other hand, the opposite is the case in the upper troposphere, where errors are particularly large for WCB outflow at early forecast stages, when pre-existing errors are mainly of small magnitude and localised. This indicates that WCBs introduce errors during their ascent, but can also amplify small-scale errors and project them onto the large-scale flow. The different complexities of the lead-time dependencies between the two variables emphasise that the mid-tropospheric errors are potentially affected by interacting and superimposed processes, such as diabatic processes and baroclinic dynamics, whereas the the upper-level wind errors follow a rather simple pattern that can be attributed fully to the diabatic outflow of WCBs.

4 | CONCLUDING DISCUSSION AND OUTLOOK

Our investigation shows that errors in medium-range forecasts of ECMWF's ensemble prediction system are associated spatially and temporally with the occurrence of WCBs. Different perspectives have been adopted to

investigate the role of WCBs for forecast errors: first, a simple stratification of forecasts based on WCB activity was used to demonstrate that forecasts with high WCB activity are characterised by reduced forecast skill compared with forecasts with low WCB activity. The separation into "good" and "bad" forecasts further indicates that the large-scale flow configurations of the two forecast classes are on average very different from each other: in the North Atlantic, forecasts with low skill are characterised by a highly amplified Rossby-wave pattern, anticyclonic flow anomalies, and strongly enhanced WCB activity, whereas good forecasts feature cyclonic anomalies over the North Atlantic and only moderate WCB activity. This serves as an illustrative example for flow-dependent predictability, which is particularly pronounced in the North Atlantic region (e.g., Ferranti *et al.*, 2015; Büeler *et al.*, 2021). Focusing on the time of largest forecast error growth demonstrates that the WCB activity is increased systematically around that time, and that WCBs amplify and redistribute pre-existing errors associated with upstream troughs and cyclogenesis. This is in line with Rodwell and Wernli (2023), who find increased forecast uncertainty around the time of cyclogenesis events in the western North Atlantic. Composites of normalised forecast errors centered spatially and lagged temporally on WCB

ascent and outflow objects further substantiate the finding that WCBs are involved in the growth and amplification of errors: coherent patterns of WCB occurrence and increased forecast errors that are associated with the representation of the Rossby-wave structure, especially in the developing jet streak north of and in the ridge downstream of WCBs, suggest a direct relationship between WCBs and forecast errors.

Even though the error patterns are clearly spatially and temporally linked to the WCB objects, the trajectory-based approach applied in this study does not allow for a direct quantification of the relative contributions of dry and moist dynamics to the error growth, as the ascending motion of the WCB includes both. Flow situations governed by baroclinic development have been shown to be characterised by similar error patterns to the ones identified in this study, as demonstrated by studies on the growth of singular vector perturbations, which emphasises the role of dry dynamics (e.g., Hoskins *et al.*, 2000). However, studies that attempt to quantify the contributions of different processes to forecast errors have shown that moist diabatic processes can have a first-order impact on tropopause-level forecast error growth (Baumgart and Riemer, 2019; Sánchez *et al.*, 2020). Further, the WCB-centered $WS250$ error patterns strongly resemble the composite of the PV tendency due to the divergent flow component for upper-level ridges (see figure 3a in Teubler and Riemer (2021)), which suggests a substantial contribution of moist dynamics to the error pattern. The importance of diabatic processes for forecast uncertainty is also considered in the design of model perturbation techniques, which often introduce noise into the parametrisation tendencies to generate ensemble spread (Leutbecher *et al.*, 2017).

Though the error patterns are very robust in the upper troposphere, the composites in the mid-troposphere are characterised by large case-to-case variability. One possible reason for these differences is that the diabatically enhanced outflow of WCBs has a stronger link to the large-scale flow than the ascent. The outflow transports low-PV air into the upper troposphere, where it diverges and sharpens the PV gradient across the tropopause. As a consequence, a jet streak forms and the waveguide is deflected northwards (Ahmadi-Givi *et al.*, 2004; Grams and Archambault, 2016). Forecast errors in that region are quickly advected by the strong jet and project onto the Rossby-wave pattern. In contrast, the WCB ascent is more confined than the outflow and quickly passes through the mid troposphere. Therefore, its link to the large-scale flow is not as direct as that of the outflow. Another aspect could be that the two variables $Z500$ and $WS250$ are not directly comparable, even though they are both commonly used to characterise the large-scale flow. Using the zonal

(U) and meridional (V) components of the wind vector at 250 hPa, however, results in very similar patterns to the wind speed (not shown). As the geopotential heights and the wind components are directly linked to each other in the free troposphere through geostrophic balance, the signal would be equivalent when using $Z250$. Nevertheless, a cleaner way would be the direct comparison of the RMSEs of $Z500$ and $Z250$, which was not feasible in the context of this study due to data availability and computing performance issues.

The three-dimensional view of the forecast errors associated with WCBs nicely illustrates that errors are propagated both horizontally and vertically: in the mid troposphere, errors that are spatially related to an upstream trough are on average already present before the WCB event occurs. In the upper troposphere, in contrast, no pre-existing errors are apparent, but large errors emerge co-located with the WCB outflow in the region of the developing jet streak and at the northwestern edge of the downstream ridge. Hence, WCBs act as a communicator between the mid-tropospheric region of enhanced and pre-existing errors and the upper-tropospheric region with originally low (or climatological) errors. The ascending motion associated with WCBs involves strong diabatic heating and cross-isentropic transport of air masses. Under adiabatic conditions, such a material transport of mass (and errors) from lower to higher isentropic levels is not possible (Saffin *et al.*, 2021). The diabatic processes involved in the WCB dynamics are therefore crucial for the growth and amplification of forecast errors, even if their immediate contribution to forecast error growth through erroneous representations of diabatic processes might be small.

Finally, it was shown that the error patterns associated with WCBs vary with lead time, and that this lead-time dependence is different between $Z500$ errors and $WS250$ errors. While WCBs that happen early in forecasts exert the largest impact on the domain-integrated errors of $WS250$, the magnitudes decrease continuously with progressing forecast lead times and are half as large as in the beginning of the forecast. Apart from the first two days, this also occurs for errors in the $Z500$ field and indicates that WCBs will have no direct impact on forecast errors at lead times well beyond the forecast times analysed in this study (e.g., at lead times in the extended range). At a stage where forecast error growth is dominated by barotropic Rossby-wave dynamics (i.e., when the Rossby-wave patterns of forecast and analysis are out of phase; Baumgart *et al.*, 2019), WCBs will not result in an additional skill reduction. These results fit into the conceptual model of upscale error growth (Zhang *et al.*, 2007), which describes a three-stage sequence in which small-scale initial errors are propagated across the scales. In the second stage, errors

on the convective scale are projected onto the synoptic scale, and it is hypothesised that diabatic processes in convection and WCBs contribute substantially to this error growth (Grams *et al.*, 2018; Selz, 2019; Selz *et al.*, 2022). Our analysis shows that WCBs project and amplify errors onto the large-scale flow, in particular in the early stages of the forecast, and thereby corroborate the findings from previous studies.

Even though this study provides strong evidence that WCBs amplify forecast errors and project them onto other scales, the methodological approach chosen here does not allow for a conclusive answer to the question of whether WCBs act as a direct source of forecast errors or as an amplifier. This requires a more sophisticated diagnostic setup, including error metrics that can be compared at different atmospheric levels. A promising approach could be to compute errors along WCB trajectories, compare errors in the inflow and outflow regions, and link the error evolution to processes that occur during the ascent of WCBs.

Future work could build on the analyses presented and generalise the findings from this study in multiple aspects: for example, one question that still remains unanswered is whether the WCB-related errors are random or systematic, which could be tackled by analysing biases. Further, the analysis could be extended to the North Pacific region and to other seasons (autumn especially, when strongly heated WCBs appear in the Northern Hemisphere ocean basins, could be interesting). Further, it would be worthwhile to perform a similar analysis for a set of different forecasting systems, such as the models in the THORPEX Interactive Grand Global Ensemble (TIGGE)[1] archive or in the context of the different models, same initial conditions project (Magnusson *et al.*, 2022). Comparing the WCB-related error structures across a range of different forecast systems could yield valuable information on how uncertainties due to moist diabatic processes depend on different model formulations, and would help to elaborate further on the question of whether WCBs primarily amplify pre-existing forecast errors or whether they act as source of uncertainty by introducing errors due to the model formulation. Such an intercomparison project based on forecast archives, however, is not feasible with a Lagrangian approach, and requires different techniques to detect WCBs in the forecasts, such as the newly developed machine-learning based approach by Quinting and Grams (2022). Wandel *et al.* (2021) provide a first attempt using such an approach and indeed also find systematic biases in WCB occurrence in the North Pacific region. Finally, all WCB objects have been considered in the same way. However, we found that the error patterns in the mid troposphere are rather complex and feature a large variability between individual cases. It could therefore be worthwhile to quantify several aspects of WCB objects and subsequently determine the related error structures. Promising characteristics are the object size, the latent heating rate along the ascent, serving as a proxy for the diabatic processes, the curvature of the outflow air mass (cyclonic versus anticyclonic), the geographical location, or the large-scale flow configuration. Such an analysis could advance our understanding of the error origins and which WCB properties and/or flow configurations are particularly prone to error growth.

AUTHOR CONTRIBUTIONS

Moritz Pickl (Deinhard): conceptualization; data curation; formal analysis; investigation; methodology; visualization; writing – original draft; writing – review and editing. **Julian F. Quinting:** data curation; supervision; writing – original draft; writing – review and editing. **Christian M. Grams:** data curation; funding acquisition; project administration; supervision; writing – original draft; writing – review and editing.

ORCID

Moritz Pickl (Deinhard) https://orcid.org/0000-0003-3853-4131
Julian F. Quinting https://orcid.org/0000-0002-8409-2541
Christian M. Grams https://orcid.org/0000-0003-3466-9389

---

[1]https://www.ecmwf.int/en/research/projects/tigge

REFERENCES

Ahmadi-Givi, F., Graig, G.C. and Plant, R.S. (2004) The dynamics of a midlatitude cyclone with very strong latent-heat release. *Quarterly Journal of the Royal Meteorological Society*, 130, 295–323.

Aiyyer, A. (2015) Recurving western North Pacific tropical cyclones and midlatitude predictability. *Geophysical Research Letters*, 42, 7799–7807.

Baumgart, M., Ghinassi, P., Wirth, V., Selz, T., Craig, G.C. and Riemer, M. (2019) Quantitative view on the processes governing the upscale error growth up to the planetary scale using a stochastic convection scheme. *Monthly Weather Review*, 147, 1713–1731.

Baumgart, M. and Riemer, M. (2019) Processes governing the amplification of ensemble spread in a medium-range forecast with large forecast uncertainty. *Quarterly Journal of the Royal Meteorological Society*, 145, 3252–3270.

Berman, J.D. and Torn, R.D. (2019) The impact of initial condition and warm conveyor belt forecast uncertainty on variability in the downstream waveguide in an ECMWF case study. *Monthly Weather Review*, 147, 4071–4089.

Bierdel, L., Selz, T. and Craig, G.C. (2018) Theoretical aspects of upscale error growth on the mesoscales: idealized numerical simulations. *Quarterly Journal of the Royal Meteorological Society*, 144, 682–694.

Binder, H., Boettcher, M., Joos, H. and Wernli, H. (2016) The role of warm conveyor belts for the intensification of extratropical cyclones in northern hemisphere winter. *Journal of the Atmospheric Sciences*, 73, 3997–4020.

Bowman, K.P., Lin, J.C., Stohl, A., Draxler, R., Konopka, P., Andrews, A. and Brunner, D. (2013) Input data requirements for Lagrangian trajectory models. *Bulletin of the American Meteorological Society*, 94, 1051–1058.

Büeler, D., Ferranti, L., Magnusson, L., Quinting, J.F. and Grams, C.M. (2021) Year-round sub-seasonal forecast skill for Atlantic-European weather regimes. *Quarterly Journal of the Royal Meteorological Society*, 147, 4283–4309.

Carlson, T.N. (1980) Airflow through midlatitude cyclones and the comma cloud pattern. *Monthly Weather Review*, 108, 1498–1509.

Chagnon, J.M., Gray, S.L. and Methven, J. (2013) Diabatic processes modifying potential vorticity in a North Atlantic cyclone. *Quarterly Journal of the Royal Meteorological Society*, 139, 1270–1282.

Choudhary, A. and Voigt, A. (2022) ICON simulations of cloud diabatic processes in the warm conveyor belt of North Atlantic cyclone Vladiana. Weather and Climate Dynamics Discussions.

Dacre, H.F. and Gray, S.L. (2013) Quantifying the climatological relationship between extratropical cyclone intensity and atmospheric precursors. *Geophysical Research Letters*, 40, 2322–2327.

Davies, H.C. and Didone, M. (2013) Diagnosis and dynamics of forecast error growth. *Monthly Weather Review*, 141, 2483–2501.

Ferranti, L., Corti, S. and Janousek, M. (2015) Flow-dependent verification of the ECMWF ensemble over the euro-Atlantic sector. *Quarterly Journal of the Royal Meteorological Society*, 141, 916–924.

Grams, C.M. and Archambault, H.M. (2016) The key role of diabatic outflow in amplifying the midlatitude flow: a representative case study of weather systems surrounding western North Pacific extratropical transition. *Monthly Weather Review*, 144, 3847–3869.

Grams, C.M., Jones, S.C. and Davis, C.A. (2013) The impact of typhoon Jangmi (2008) on the midlatitude flow. Part II: downstream evolution. *Quarterly Journal of the Royal Meteorological Society*, 139, 2165–2180.

Grams, C.M., Magnusson, L. and Madonna, E. (2018) An atmospheric dynamics perspective on the amplification and propagation of forecast error in numerical weather prediction models: a case study. *Quarterly Journal of the Royal Meteorological Society*, 144, 2577–2591.

Grams, C.M., Wernli, H., Böttcher, M., Čampa, J., Corsmeier, U., Jones, S.C., Keller, J.H., Lenz, C.J. and Wiegand, L. (2011) The key role of diabatic processes in modifying the upper-tropospheric wave guide: a North Atlantic case-study. *Quarterly Journal of the Royal Meteorological Society*, 137, 2174–2193.

Hartigan, J. and Wong, M. (1979) Algorithm AS 136: a k-means clustering algorithm. *Journal of the Royal Statistical Society Series C*, 28, 100–108.

Hoskins, B.J., Buizza, R. and Badger, J. (2000) The nature of singular vector growth and structure. *Quarterly Journal of the Royal Meteorological Society*, 126, 1565–1580.

Joos, H. and Forbes, R.M. (2016) Impact of different IFS microphysics on a warm conveyor belt and the downstream flow evolution. *Quarterly Journal of the Royal Meteorological Society*, 142, 2727–2739.

Leutbecher, M., Lock, S.J., Ollinaho, P., Lang, S.T., Balsamo, G., Bechtold, P., Bonavita, M., Christensen, H.M., Diamantakis, M., Dutra, E., English, S., Fisher, M., Forbes, R.M., Goddard, J., Haiden, T., Hogan, R.J., Juricke, S., Lawrence, H., MacLeod, D., Magnusson, L., Malardel, S., Massart, S., Sandu, I., Smolarkiewicz, P.K., Subramanian, A., Vitart, F., Wedi, N. and Weisheimer, A. (2017) Stochastic representations of model uncertainties at ECMWF: state of the art and future vision. *Quarterly Journal of the Royal Meteorological Society*, 143, 2315–2339.

Madonna, E., Boettcher, M., Grams, C.M., Joos, H., Martius, O. and Wernli, H. (2015) Verification of North Atlantic warm conveyor belt outflows in ECMWF forecasts. *Quarterly Journal of the Royal Meteorological Society*, 141, 1333–1344.

Madonna, E., Li, C. and Wettstein, J.J. (2019) Suppressed eddy driving during southward excursions of the North Atlantic jet on synoptic to seasonal time scales. *Atmospheric Science Letters*, 20, e937.

Madonna, E., Limbach, S., Aebi, C., Joos, H., Wernli, H. and Martius, O. (2014a) On the co-occurrence of warm conveyor belt outflows and PV streamers. *Journal of the Atmospheric Sciences*, 71, 3668–3673.

Madonna, E., Wernli, H., Joos, H. and Martius, O. (2014b) Warm conveyor belts in the ERA-interim dataset (1979–2010). Part I: climatology and potential vorticity evolution. *Journal of Climate*, 27, 3–26.

Magnusson, L., Ackerley, D., Bouteloup, Y., Chen, J.H., Doyle, J., Earnshaw, P., Kwon, Y.C., Köhler, M., Lang, S.T., Lim, Y.J., Matsueda, M., Matsunobu, T., McTaggart-Cowan, R., Reinecke, A., Yamaguchi, M. and Zhou, L. (2022) Skill of medium-range forecast models using the same initial conditions. *Bulletin of the American Meteorological Society*, 103, 2050–2068.

Martínez-Alvarado, O., Gray, S.L. and Methven, J. (2016a) Diabatic processes and the evolution of two contrasting summer extratropical cyclones. *Monthly Weather Review*, 144, 3251–3276.

Martínez-Alvarado, O., Madonna, E., Gray, S.L. and Joos, H. (2016b) A route to systematic error in forecasts of Rossby waves. *Quarterly Journal of the Royal Meteorological Society*, 142, 196–210.

Mazoyer, M., Ricard, D., Rivière, G., Delanoë, J., Arbogast, P., Vié, B., Lac, C., Cazenave, Q. and Pelon, J. (2021) Microphysics impacts

on the warm Conveyor Belt and ridge building of the NAWDEX IOP6 cyclone. *Monthly Weather Review*, 149, 3961–3980.

Methven, J. (2015) Potential vorticity in warm conveyor belt outflow. *Quarterly Journal of the Royal Meteorological Society*, 141, 1065–1071.

Oertel, A., Pickl, M., Quinting, J.F., Hauser, S., Wandel, J., Magnusson, L., Balmaseda, M., Vitart, F. and Grams, C.M. (2023) Everything hits at once: how remote rainfall matters for the prediction of the 2021 north American heat wave. *Geophysical Research Letters*, 50, e2022GL100958.

Pfahl, S., Madonna, E., Boettcher, M., Joos, H. and Wernli, H. (2014) Warm conveyor belts in the ERA-interim dataset (1979–2010). Part II: moisture origin and relevance for precipitation. *Journal of Climate*, 27, 27–40.

Pfahl, S., Schwierz, C., Croci-Maspoli, M., Grams, C.M. and Wernli, H. (2015) Importance of latent heat release in ascending air streams for atmospheric blocking. *Nature Geoscience*, 8, 610–614.

Pickl, M., Lang, S.T., Leutbecher, M. and Grams, C.M. (2022) The effect of stochastically perturbed parametrisation tendencies (SPPT) on rapidly ascending air streams. *Quarterly Journal of the Royal Meteorological Society*, 148, 1242–1261.

Pomroy, H.R. and Thorpe, A.J. (2000) The evolution and dynamical role of reduced upper-tropospheric potential vorticity in intensive observing period one of FASTEX. *Monthly Weather Review*, 128, 1817–1834.

Quinting, J.F. and Grams, C. (2022) EuLerian identification of ascending air streams (ELIAS 2.0) in numerical weather prediction and climate models. Part I: development of deep learning model. *Geoscientific Model Development*, 15, 715–730.

Quinting, J.F. and Grams, C.M. (2021) Toward a systematic evaluation of warm conveyor belts in numerical weather prediction and climate models. Part I: predictor selection and logistic regression model. *Journal of the Atmospheric Sciences*, 78, 1465–1485.

Quinting, J.F., Grams, C.M., Oertel, A. and Pickl, M. (2022) EuLerian identification of ascending AirStreams (ELIAS 2.0) in numerical weather prediction and climate models–part 2: model application to different datasets. *Geoscientific Model Development*, 15, 731–744.

Quinting, J.F. and Jones, S.C. (2016) On the impact of tropical cyclones on Rossby wave packets: a climatological perspective. *Monthly Weather Review*, 144, 2021–2048.

Rivière, G., Wimmer, M., Arbogast, P., Piriou, J.-M., Delanoë, J., Labadie, C., Cazenave, Q. and Pelon, J. (2021) The impact of deep convection representation in a global atmospheric model on the warm conveyor belt and jet stream during NAWDEX IOP6. *Weather and Climate Dynamics*, 2, 1011–1031.

Rodwell, M.J., Magnusson, L., Bauer, P., Bechtold, P., Bonavita, M., Cardinali, C., Diamantakis, M., Earnshaw, P., Garcia-Mendez, A., Isaksen, L., Källén, E., Klocke, D., Lopez, P., McNally, T., Persson, A., Prates, F. and Wedi, N. (2013) Characteristics of occasional poor medium-range weather forecasts for Europe. *Bulletin of the American Meteorological Society*, 94, 1393–1405.

Rodwell, M.J. and Wernli, H. (2023) Uncertainty growth and forecast reliability during extratropical cyclogenesis. *Weather and Climate Dynamics*, 4, 591–615.

Röthlisberger, M., Martius, O. and Wernli, H. (2018) Northern hemisphere Rossby wave initiation events on the extratropical jet-a climatological analysis. *Journal of Climate*, 31, 743–760.

Saffin, L., Methven, J., Bland, J., Harvey, B. and Sanchez, C. (2021) Circulation conservation in the outflow of warm conveyor belts and consequences for Rossby wave evolution. *Quarterly Journal of the Royal Meteorological Society*, 147, 3587–3610.

Sánchez, C., Methven, J., Gray, S. and Cullen, M. (2020) Linking rapid forecast error growth to diabatic processes. *Quarterly Journal of the Royal Meteorological Society*, 146, 3548–3569.

Schäfler, A. and Harnisch, F. (2015) Impact of the inflow moisture on the evolution of a warm conveyor belt. *Quarterly Journal of the Royal Meteorological Society*, 141, 299–310.

Selz, T. (2019) Estimating the intrinsic limit of predictability using a stochastic convection scheme. *Journal of the Atmospheric Sciences*, 76, 757–765.

Selz, T., Riemer, M. and Craig, G. (2022) The transition from practical to intrinsic predictability of midlatitude weather. *Journal of the Atmospheric Sciences*, 79, 2013–2030.

Sprenger, M., Fragkoulidis, G., Binder, H., Croci-Maspoli, M., Graf, P., Grams, C.M., Knippertz, P., Madonna, E., Schemm, S., Škerlak, B. and Wernli, H. (2017) Global climatologies of Eulerian and Lagrangian flow features based on ERA-interim. *Bulletin of the American Meteorological Society*, 98, 1739–1748.

Sprenger, M. and Wernli, H. (2015) The LAGRANTO Lagrangian analysis tool–version 2.0. *Geoscientific Model Development*, 8, 2569–2586.

Steinfeld, D., Boettcher, M., Forbes, R. and Pfahl, S. (2020) The sensitivity of atmospheric blocking to upstream latent heating–numerical experiments. *Weather and Climate Dynamics*, 1, 405–426.

Steinfeld, D. and Pfahl, S. (2019) The role of latent heating in atmospheric blocking dynamics: a global climatology. *Climate Dynamics*, 53, 6159–6180.

Teubler, F. and Riemer, M. (2021) Potential-vorticity dynamics of troughs and ridges within Rossby wave packets during a 40-year reanalysis period. *Weather and Climate Dynamics*, 2, 535–559.

Wandel, J., Quinting, J.F. and Grams, C.M. (2021) Toward a systematic evaluation of warm conveyor belts in numerical weather prediction and climate models. Part II: verification of operational reforecasts. *Journal of the Atmospheric Sciences*, 78, 3965–3982.

Wernli, H. (1997) A Lagrangian-based analysis of extratropical cyclones. II: a detailed case-study. *Quarterly Journal of the Royal Meteorological Society*, 123, 1677–1706.

Wernli, H. and Davies, H.C. (1997) A Lagrangian-based analysis of extratropical cyclones. I: the method and some applications. *Quarterly Journal of the Royal Meteorological Society*, 123, 467–489.

Zhang, F., Bei, N., Rotunno, R., Snyder, C. and Epifanio, C.C. (2007) Mesoscale predictability of moist baroclinic waves: convection-permitting experiments and multistage error growth dynamics. *Journal of the Atmospheric Sciences*, 64, 3579–3594.

SUPPORTING INFORMATION

Additional supporting information can be found online in the Supporting Information section at the end of this article.